Chapter 5

Chapter 5

Design, Synthesis, and Biological Evaluation of Indole and Piperazine-Substituted Ketoamides as Potential Protein Aggregation Modulators

5.1. Introduction

Indole is an aromatic heterocyclic organic compound with the formula C_8H_7N. It is composed of a benzene ring fused to a five-membered pyrrole ring. This bicyclic structure is prevalent in many natural products and pharmaceuticals [1]. While their role in AD is still an area of ongoing research, some indole derivatives have shown potential in various aspects related to AD. Indole-3-acetic acid (IAA) is a naturally occurring plant hormone that has been studied for its potential neuroprotective effects. It has been shown to protect against neurotoxicity induced by Aβ. IAA also exhibits antioxidant and anti-inflammatory properties, which may contribute to its neuroprotective effects [2, 3]. Indole-3-carbinol (I3C) is a compound found in cruciferous vegetables such as broccoli, cauliflower, and cabbage. It has been investigated for its ability to modulate certain signaling pathways involved in AD pathogenesis. Studies have suggested that I3C can inhibit the production and aggregation of Aβ and tau proteins, which are implicated in AD [4]. Indoleamine 2,3-dioxygenase (IDO) is an enzyme involved in the metabolism of the amino acid tryptophan. In AD, IDO activity has been linked to neuroinflammation and the production of neurotoxic metabolites [5]. Inhibiting IDO activity may have potential therapeutic benefits. Some indole derivatives have been studied as IDO inhibitors and have shown promise in reducing neuroinflammation and improving cognitive function in animal models of AD. Indirubins are naturally occurring compounds derived from indole that have been investigated for their potential anti-AD properties [6]. Inhibiting GSK-3β could potentially prevent or slow down the progression of AD. In 2018, Oscar et. al., introduced a molecule

named Contilisant which demonstrated antioxidant and neuroprotective properties along with good permeability. The study highlighted its high affinity in the nM range for H3R and its superior inhibitory effects on monoamine oxidases and cholinesterases. It was also observed that Contilisant could reverse cognitive deficits caused by $A\beta_{42}$ in a radial maze assay, a test relevant to AD [7]. It's important to note that while these indole derivatives have shown promise in preclinical studies, further research is needed to evaluate their efficacy, safety, and potential for clinical use in AD.

The piperazine bearing a nitro substituted phenyl ring has been playing a key motif in drug medicinal chemistry [8, 9]. The nitro group's electron-withdrawing nature on the phenyl ring can influence the electron density on both the phenyl and piperazine rings, rendering the entire molecule more electrophilic. Such electron-withdrawing effects often impact the molecule's overall reactivity and can modify its interactions with biological targets. One of the proposed mechanisms of action for nitro piperazine in AD is its ability to inhibit the activity of AChE [10]. By inhibiting AChE, nitro piperazine may increase the levels of acetylcholine in the brain, potentially improving cognitive function and memory in AD [10, 11]. In addition to its AChE inhibitory activity, nitrophenyl substituted piperazine has also been shown to have antioxidant and anti-inflammatory properties [12]. Oxidative stress and inflammation are both implicated in the pathogenesis of AD, and reducing these processes may help to slow the progression of the disease. Overall, while research on the role of nitropiperazine in AD is still in its early stages, the compounds containing nitropiperazine ring act as a potential therapeutic agent for the treatment of AD.

In our initial study (**Chapter 3**), we established that compound 1 exhibits promising potential as a protein modulator by expediting the process of Aβ aggregation. Subsequently, in our second study (**Chapter 4**), we discerned that various derivatives of piperazine and piperidine possess the capability to modulate protein aggregation. Among these derivatives, compound

BD23 was identified as a lead molecule, demonstrating an enhanced capacity to promote the aggregation of Aβ. Notably, our in vivo experiments provided compelling evidence that BD23 has the capacity to ameliorate cognitive function in the context of Aβ aggregation.

Motivated by these encouraging findings, our research trajectory led us to undertake further investigations. So in this study, we embarked on the synthesis of various indole and piperazine substituted α-ketoamides derivatives, with the overarching objective of gaining deeper insights into the efficacy of α-ketoamides in mitigating protein aggregation in AD.

5.2. Objectives

The objectives of this study are as follows:

- **Compound synthesis and characterization:** To synthesize different indole and piperazine substituted α-ketoamides and determine their structural properties through NMR spectroscopy, Mass spectrometry.
- **In vitro Aβ aggregation assay:** To investigate the potential of all α-ketoamides as an Aβ aggregation modulators, assessing its inhibition of Aβ aggregation using ThT assay.
- **Physicochemical evaluation of hit compounds:** To ensure that the hit compounds meet the necessary physicochemical criteria for effective drug candidates, considering their solubility and BBB permeability as crucial factors in drug development.
- **In vitro heparin-induced tau aggregation assay:** To investigate the potential of the lead compound in preventing or reducing tau protein clumping triggered by heparin.
- **In vitro cytotoxicity assay:** To perform the in vitro cytotoxicity assay for the purpose of assessing the cytotoxic properties of specific hit molecules.
- **In vivo behavioral studies of the compound in Aβ-induced cognitive deficit mice model:** To evaluate the impact of the lead compound on cognitive function in the Aβ-induced cognitive deficit mice model.
- **In silico studies:** To perform molecular docking against Aβ peptide monomer and fibril

structure as well as tau peptide followed by molecular dynamics simulation to evaluate the binding mode of the compound with the target. Utilize DFT calculation calculations to analyze the electronic structure, stability, and reactivity of the hit compound, including optimizing its stable structure and identifying reactive sites.

5.3. Result and Discussion

5.3.1. Chemistry

The different substituted novel indole and piperazine derivatives were synthesized by using previously reported methods [13, 14]. Different substituted benzylidene acetone synthesized by interactions with Wittig salt (1-(Triphenylphosphoranylidene)-2-propanone). Furthermore, the intermediates were reacted with PPh_3HBr in the presence of DMSO at 50 °C produced β,γ-unsaturated-α- ketothisoesters. The intermediates further underwent chemoselective reduction in the presence of Et_3SiH and BF_3OEt_2 as Lewis catalyst in DCM at inert conditions produced β,γ-unsaturated-α-hydroxythioesters. Then the different substituted β,γ-unsaturated-α-hydroxythisoesters reacted with different indole and piperazine substituted amines and produced indole and piperazine α-ketoamides. **Table 5.1** and **Table 5.2** shows the structure of twenty-four synthesized compounds.

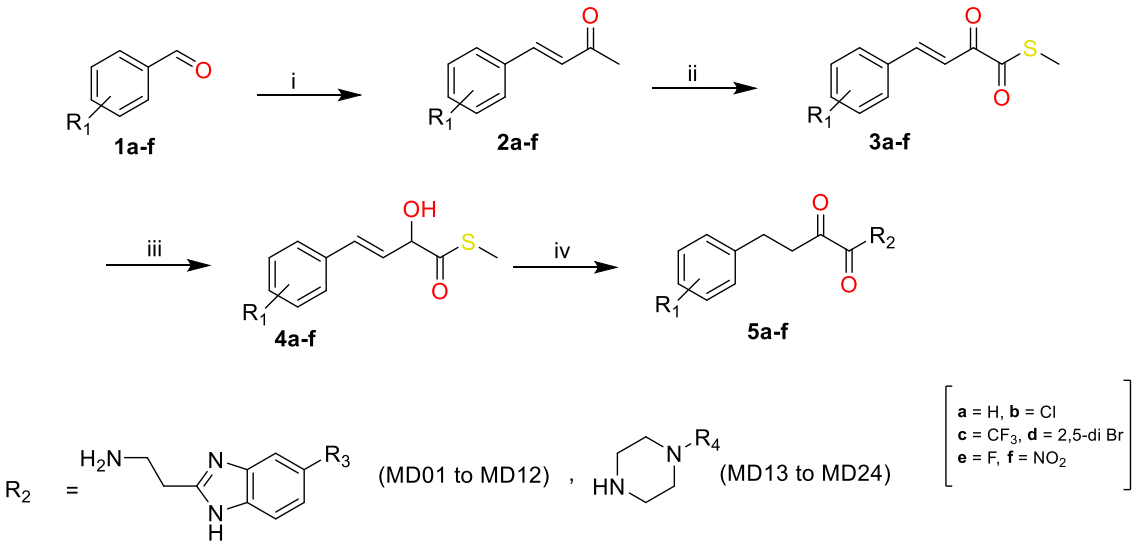

Scheme 5.1. Synthesis of novel indole and piperazine α-ketoamide (MD01-MD24). (i)

Wittig salt (1-(Triphenylphosphoranylidene)-2-propanone), THF, 6-48 hrs (ii) PPh_3.HBr, DMSO, 50 °C (iii) Et_3SiH, BF_3OEt, dry DCM, rt (iv) Amines, dry DCM, rt

Table 5.1. Structures of the synthesized indole substituted α-ketoamides (MD01-MD12).

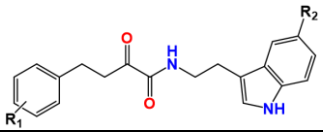

Compound ID	R_1	R_2
MD01	H	H
MD02	H	-OMe
MD03	4-Cl	H
MD04	4-Cl	-OMe
MD05	2-F	H
MD06	2-F	-OMe
MD07	2,5-di Br	H
MD08	2,5-di Br	-OMe
MD09	4-CF_3	H
MD10	4-CF_3	-OMe
MD11	4-NO_2	H
MD12	4-NO_2	-OMe

Table 5.2. Structures of the synthesized piperazine substituted α-ketoamides (MD13 to MD24).

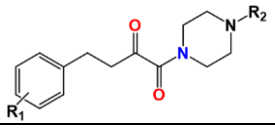

Compound ID	R_1	R_2	Compound ID	R_1	R_2
MD13	H	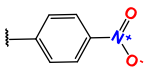	MD19	2-F	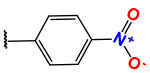
MD14	H	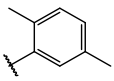	MD20	2-F	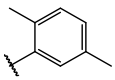
MD15	H	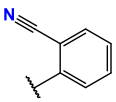	MD21	2-F	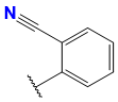
MD16	4-Cl	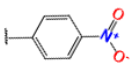	MD22	3-NO_2	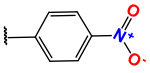
MD17	2,5-di Br	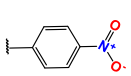	MD23	3-NO_2	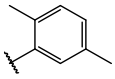
MD18	4-CF_3	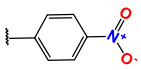	MD24	3-NO_2	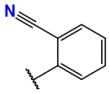

5.3.2. In vitro Aβ aggregation assay and Structure Activity Relationship study

The synthesized compounds (**MD01-MD24**) were tested for their effect on the Aβ aggregation using ThT assay. From the results of the Aβ aggregation assay, it was observed that many of the compounds showed modulation of Aβ aggregation as indicated by the increase in the lag phase of the Aβ aggregation kinetics as shown in **Figure 5.1**.

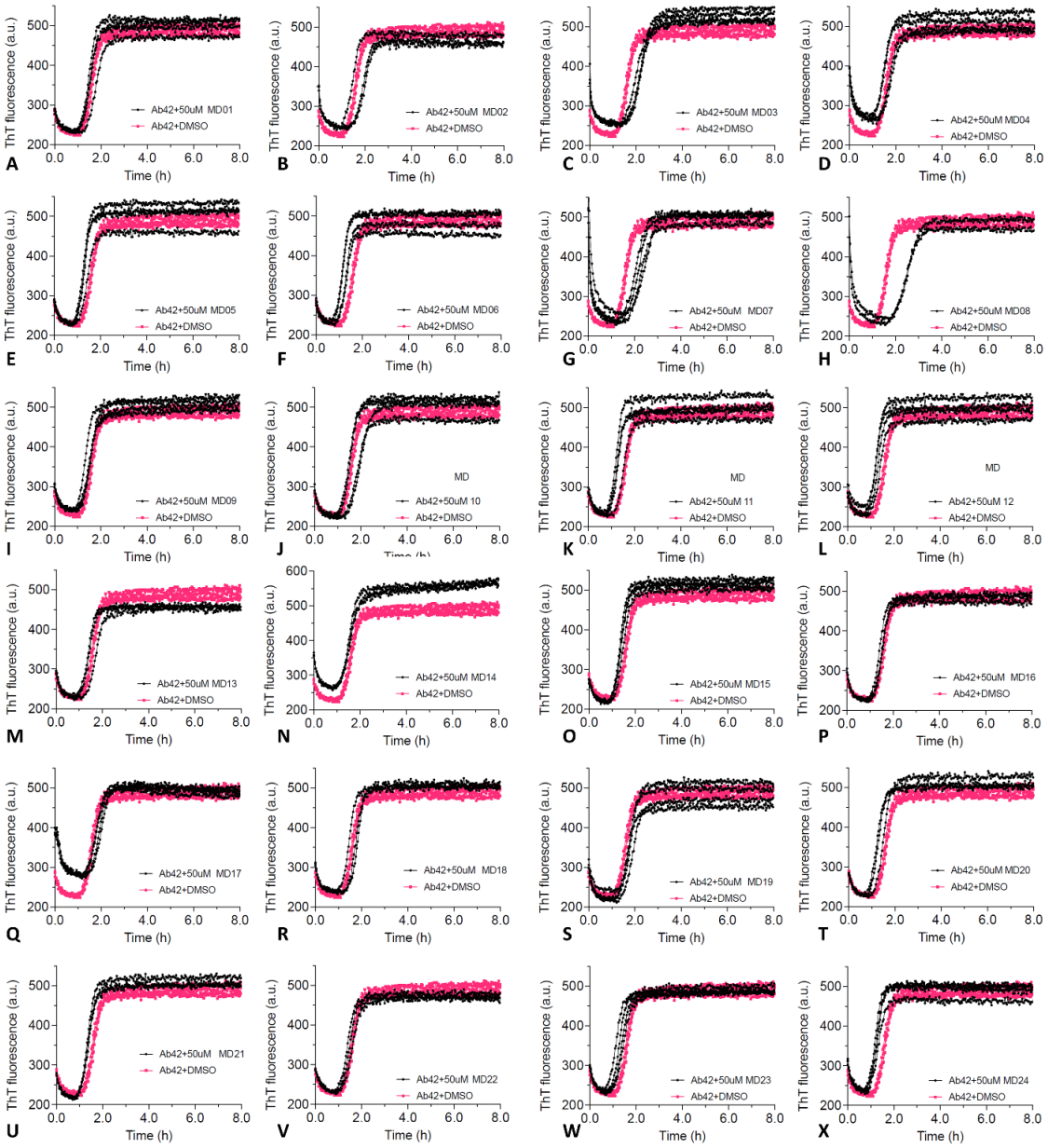

Figure 5.1. Aβ aggregation kinetics in the presence of compounds MD01-MD24. Figure 2A to 2AB represents the Aβ aggregation kinetics in the presence of 50 µM of the compound MD01 to MD24, respectively. The red graph indicates the ThT fluorescence of the compound well and

the black graph represents the ThT fluorescence of the residual DMSO in reaction buffer equivalent to the amount of DMSO in the compound well.

In order to assess the modulation effect, we calculated the aggregation half-time (τ1/2) for all the compounds and compared it to the control group ($A\beta_{42}$+ DMSO). Most of the compounds exhibited an extension in the τ1/2, indicating a slowdown in the kinetics of Aβ aggregation. Interestingly, compound MD08 displayed a reduction in the τ1/2, suggesting its pro-aggregation influence. Based on the observed τ1/2 increases, we identified compounds MD03, MD07, MD08, and MD10 as potential hit compounds and proceeded with further evaluation.

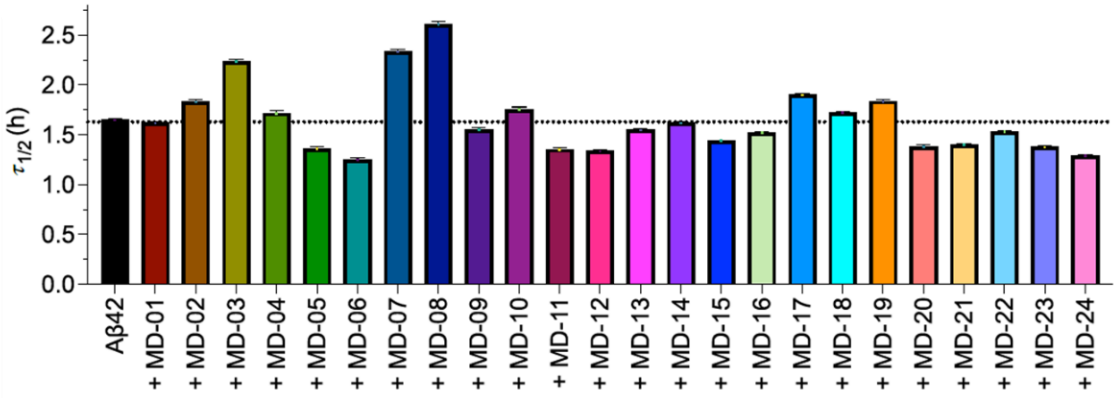

Figure 5.2. Aggregation half-time ($\tau_{1/2}$) of the compounds (MD01-MD24). Aggregation half-time ($\tau_{1/2}$) determined by fitting the fibrillization traces of the $A\beta_{42}$ peptide with to a sigmoidal equation given by Eq. ($F=F0+A/(1+\exp[rmax\ (\tau 1/2-t)]$) where *A* the amplitude and F_0 the base value.

The structure-activity relationship of the synthesized α-ketoamides has been elucidated in the **Figure 5.4**. It was observed that the substitution of a halogen atom, especially at the R_1 and R_3 positions, augments the compound's potency. Conversely, the introduction of a NO_2 group at the R_4 position diminishes the potency. Interestingly, replacing the R_4 position with a methoxy group enhances the potency. Furthermore, when the R_2 group in ring A is substituted with a chlorine atom, the potency increases; however, trifluoromethyl (CF_3) substitution demonstrates

greater potency compared to the chlorine atom (Cl).

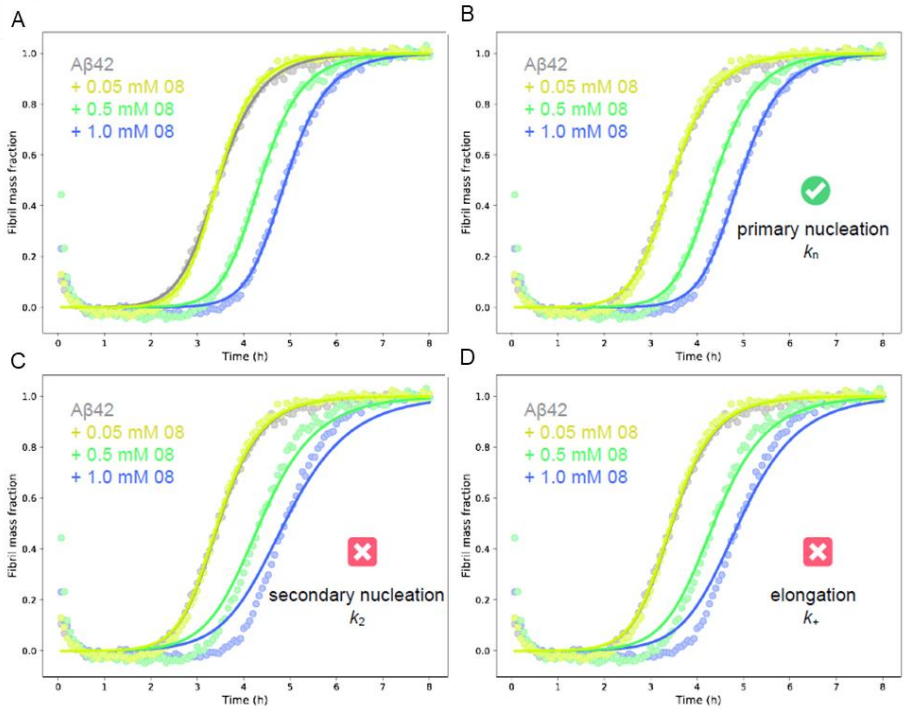

Figure 5.3. Protein aggregation inhibition (A-D) obtained from the global fitting of kinetic models shows that compound MD08 is well fitted for inhibition of primary nucleation. The compound is not well-fitted with secondary nucleation (C) and elongation (D).

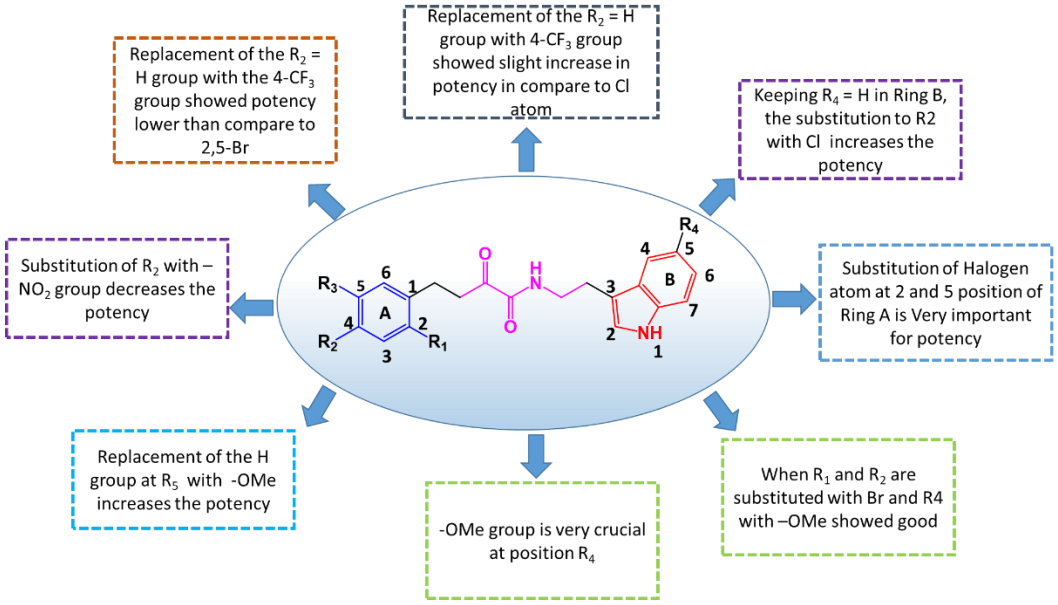

Figure 5.4. Structural Activity Relationship (SAR) study of compounds (MD01-MD24) based on their effect on Aβ aggregation kinetics.

5.3.3. Solubility Study of the Hit Compounds

In order to evaluate the solubility of the hit compounds we performed a kinetic solubility study of MD03, MD07, MD08, and MD10. **Table 5.3** shows the solubility results for which indicates that the solubility of these compounds are ranging between 0.037 to 0.048 mg/mL.

Table 5.3. Solubility data of four hit compounds.

Compound	Solubility (mg/mL) Mean ± SD (N=3)	Percent Purity (%)	cLogP*
MD03	0.048 ± 0.0038	96.48	4.364
MD07	0.039 ± 0.0029	95. 12	5.377
MD08	0.037 ± 0.0035	97.02	5.398
MD10	0.045 ± 0.0042	98.32	4.555

*Calculated using RDKit algorithm

5.3.4. In Vitro Blood Brain Barrier Permeability Study of the Compound MD08

The BBB-permeability of potential lead compound MD08 was assessed by using PAMPA-BBB assay and compared with positive control, negative control, and standard drug DPZ. The permeability coefficient rate obtained for the compound MD08 was $2.22 \pm 0.70 \times 10^{-6}$ cm s^{-1} as depicted in the **Table 5.4**.

Table 5.4: PAMPA-BBB permeability of compound MD08. (PC: Positive Control, NC: Negative Control).

Compound	Permeability Rate (Pe) ($\times 10^{-6}$ cm s^{-1}) Mean ± SD (N=2)
MD08	2.22 ± 0.70
Promazine Hydrochloride (PC)	6.83 ± 0.82
Diclofenac (NC)	3.32 ± 0.48
Donepezil (PC)	13.8 ± 13.7

5.3.5. Compound MD08 Inhibited Heparin-induced Tau Aggregation

To elucidate the protein modulation capabilities of the lead compound, we assessed its activity in countering tau aggregation using the ThT-based assay. Specifically, we employed the heparin-induced tau aggregation method. As depicted in **Figure 5.5**, tau, upon incubation with heparin, exhibits a complete (100%) aggregation propensity. Our empirical findings highlight that, in the presence of compound MD08 at a concentration of 100 µM during the co-incubation process with tau and heparin, there is a pronounced reduction in tau aggregation. In a stark comparison, by augmenting the concentration of compound MD08 to 200 µM, we observed an even more significant inhibitory effect, leading to a further decline in tau aggregation.

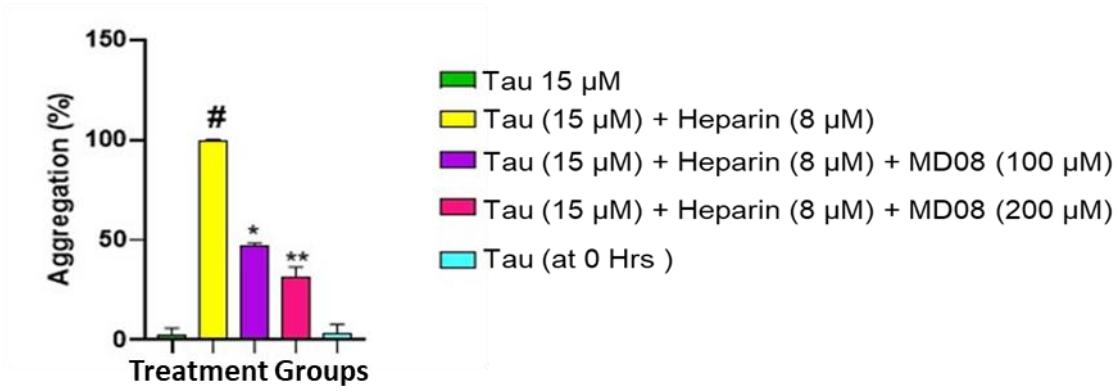

Figure 5.5. Effect of compound MD08 on tau aggregation monitored by ThT after 72 hrs incubation at 37 °C. The # represents significance compared to the MD08 untreated control group (tau + heparin). Data were expressed as Mean ± SEM and analyzed by one-way ANOVA (Tukey's multiple comparisons test) (n=2). ***p<0.001), **p<0.01, *p<0.05. Ns non-significant p-value.

5.3.6. In vitro Cytotoxicity Assay

For cytotoxicity evaluation, compounds MD02. MD03, MD07, MD08, MD19 at 50 µM were incubated with the SH-SY5Y cells for 24 hours and the metabolic activity of the cells was evaluated using MTT assay. The results indicated that compounds MD03, MD07, MD08, and MD10 did not manifest any cytotoxic effects when juxtaposed against the control group.

Notably, compound MD02 deviated from this pattern, exhibiting an enhancement in cell proliferation. The percentage of cell viability of each compound is represented in the **Figure 5.6.** Microscopic images didn't show any major changes in the cell morphology after treatment with the compounds **(Figure 5.7)**.

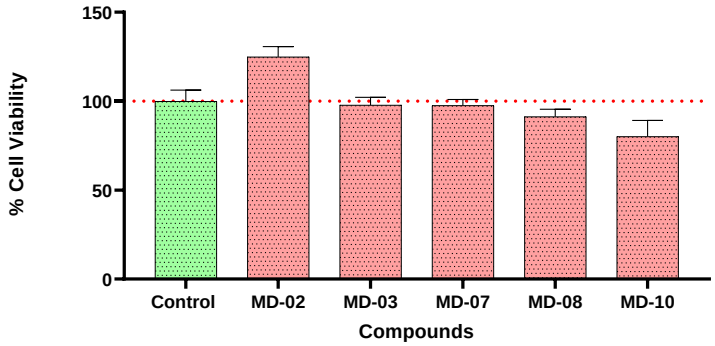

Figure 5.6. Histograms of the viability of SH-SY5Y cells upon the treatment with different compounds at 50 µM concentrations for 24 hrs. Data were expressed as Mean ± SEM and analyzed by one-way ANOVA (Tukey's multiple comparisons) (n=6). **** represents significance compared to the control group ($p<0.0001$), ns- not significant.

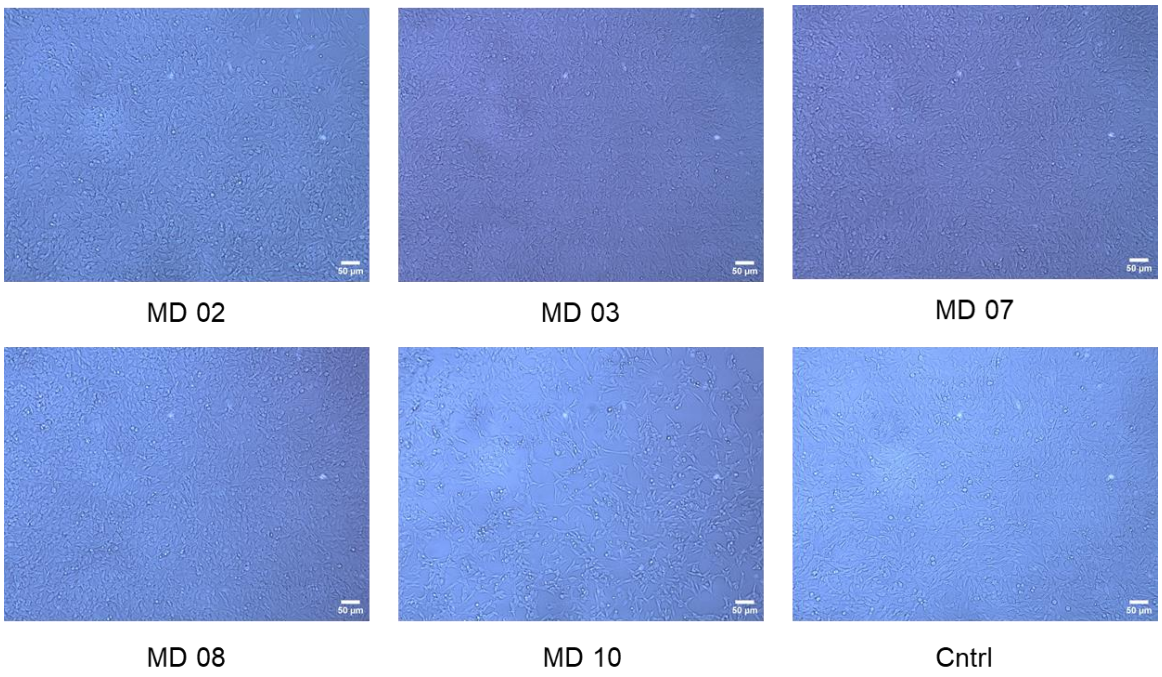

Figure 5.7. Morphological changes of SHSY-5Y cells as observed under an inverted light microscope (10× magnification). The scale bar is of 50 µM.

5.3.7. In Vivo Behavioral Studies of Compound MD08 in Aβ-Induced Cognitive Deficit Mice Model

5.3.7.1. MD08 improved the learning & and memory impairment in Aβ-Induced Cognitive Deficit Mice Model in Elevated Plus Maze test

In order to determine the learning and memory in mice we have performed EPM and calculated the percentage of the initial percentage of latency. The naive group showed lower percentage of initial transfer latency as compared to Aβ treated group. The group treated with compound MD08 at a dose of 2 mg/kg bodyweight showed decrease in initial percentage of latency non-significantly which is around 45 %. The molecule showed less significant effect by decreasing the initial transfer latency (40%) at a dose of 5mg/kg as compare to disease control group. When the dose is increased to 10 mg/kg, the treatment group showed a significant reduction in initial transfer latency to 25 % which is slightly more than the standard drug donepezil, represented in **Figure 5.8.** The result suggested that the compound improved the cognitive function in the injected mice model at 10 mg/kg dose**.**

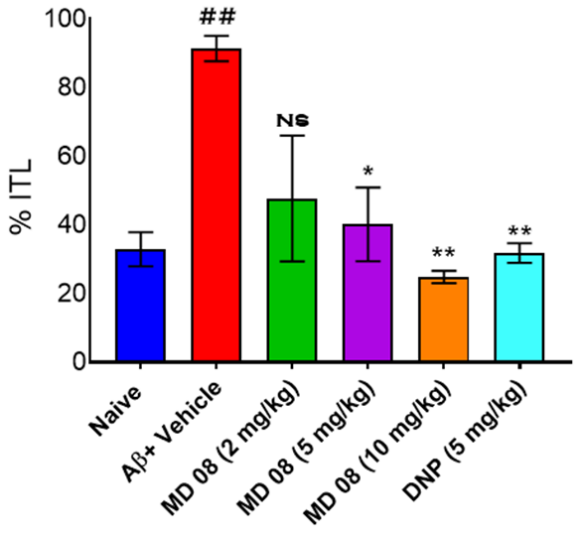

Figure 5.8. Effect of MD08 on % Initial Transfer Latency (% ITL). MD08 administration significantly improved the % ITL in $A\beta_{25-35}$ Injected Mice. Data were expressed as Mean ± SEM and analyzed by one-way ANOVA (Tukey's multiple comparisons) (n=5). ## represents

significance compared to the control group ($p<0.05$), * ($p<0.05$), ** ($p<0.01$) represents significance compared to the vehicle group. MD08 doses (2, 5 & 10 mg/kg i.p), Donepezil (DNP- 5mg/kg i.p).

5.3.7.2. MD08 increased the discrimination ratio in Aβ injected mice in a novel object recognition test

In order to investigate the effect of MD08 in improving recognition memory in Aβ injected mice we performed novel object recognition test by comparing standard drug DNP**. Figure 5.9** shows the discrimination index of different dose-treated groups with a disease control group and standard drug Donepezil. The compound MD08 at a dose 2 mg/kg administration in $A\beta_{25-35}$ injected mice showed no significant effect in improving discrimination index, when the dose was increased to 5 mg and 10 mg/kg, the effect was significant indicating that the compounds MD08 at 5 and 10 mg/kg dose can improve cognitive function.

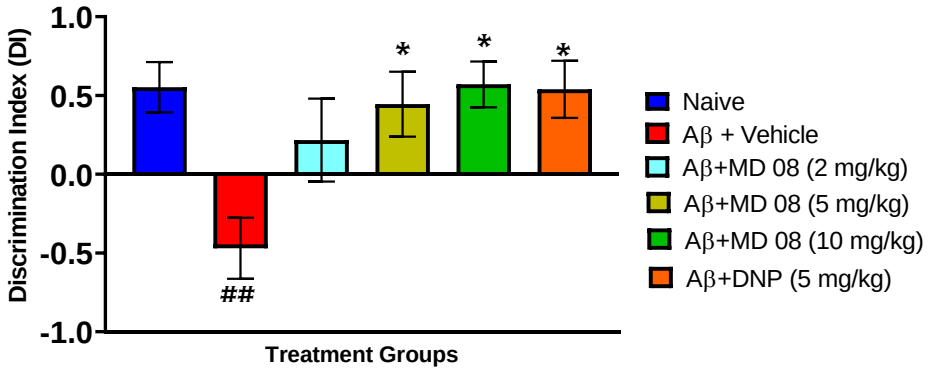

Figure 5.9. **Effect of MD08 on Discrimination Ratio in Novel Object Recognition Test.** MD08 administration in $A\beta_{25-35}$ injected mice significantly improved the discrimination index. Data were expressed as Mean ± SEM and analyzed by one-way ANOVA (Tukey's multiple comparisons) (n=5). ## represents significance compared to the control group ($p<0.05$), * ($p<0.05$), ** ($p<0.01$) represents significance compared to the vehicle group. MD08 doses (2, 5 & 10 mg/kg i.p), Donepezil (DNP- 5 mg/kg i.p).

5.3.7.3. MD08 did not affect motor coordination in $A\beta_{25-35}$ injected mice in Rotarod test.

We have performed rotarod test of the animals group treated with MD08 at a dose of 10 mg/kg and compared it with the Aβ saline-injected group and standard drug DPZ. No significant difference was observed between these three groups suggesting that the lead molecule MD08 did not affect motor coordination **(Figure 5.10**).

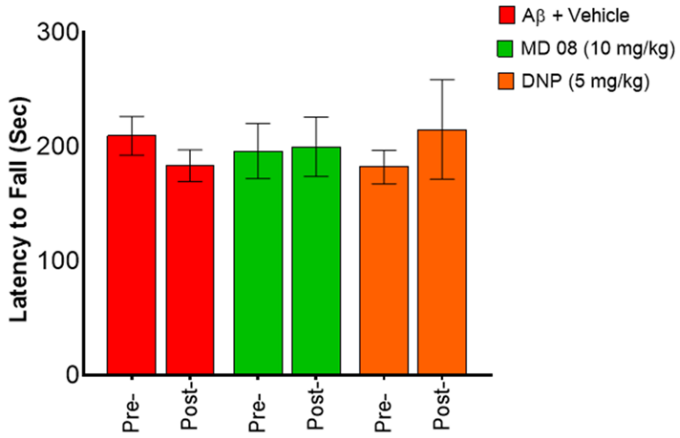

Figure 5.10. MD08 did not affect motor coordination in $A\beta_{25-35}$ injected mice. MD08 administration in $A\beta_{25-35}$ injected mice showed no sign of motor incoordination in the rotarod test. Data were expressed as Mean ± SEM and analyzed by one-way ANOVA (Tukey's multiple comparisons) (n=5). # represents significance compared to the control group ($p<0.05$), * ($p<0.05$), ** ($p<0.01$) represents significance compared to the vehicle group. MD-08 dose (10 mg/kg i.p), Donepezil (DNP- 5mg/kg i.p)

5.3.8. In silico Molecular Docking Study

Molecular docking studies were conducted on all the twenty-four synthesized compounds utilizing both the Aβ monomer (PDB: 1IYT) and pentamer (PDB: 2BEG) structures. Additionally, the docking interactions with the tau protein, specifically cluster 06 and cluster 08, were meticulously examined. The docking score obtained in the study is given in **Table 5.5.**

Table 5.5. Molecular docking score of the compounds (MD01-BD24) against Aβ monomer (PDB ID:1IYT), Aβ fibril (PDB:2BEG) and tau monomers (Cluster 6 and Cluster 8).

Compound	1IYT			2BEG			Cluster 6			Cluster 8		
	Affinity (Kcal/mol)	CNN Score	CNN Affinity	Affinity (Kcal/mol)	CNN Score	CNN Affinity	Affinity (Kcal/mol)	CNN Score	CNN Affinity	Affinity (Kcal/mol)	CNN Score	CNN Affinity
MD01	-5.786	0.859	4.263	-6.384	0.615	5.546	-7.297	0.392	4.809	-7.883	0.618	4.8
MD02	-4.128	0.693	4.556	-4.78	0.579	5.524	-4.812	0.424	3.713	-7.019	0.673	5.24
MD03	-4.326	0.708	4.339	-5.447	0.668	5.847	-7.127	0.584	5.188	-8.658	0.589	5.499
MD04	-4.436	0.63	4.327	-4.346	0.56	5.731	-4.72	0.368	4.802	-5.948	0.378	4.953
MD05	-5.538	0.711	4.247	-5.57	0.694	4.829	-4.745	0.545	4.716	-7.011	0.48	5.032
MD06	-4.151	0.604	4.591	-4.825	0.64	5.772	-5.85	0.373	4	-8.499	0.701	5.498
MD07	-4.776	0.65	5.16	-6.643	0.704	5.56	-5.001	0.345	4.424	-7.068	0.652	5.431
MD08	-4.315	0.629	4.769	-6.202	0.807	6.148	-4.389	0.414	5.005	-6.922	0.618	5.504
MD09	-3.818	0.538	4.93	-4.491	0.621	5.792	-8.825	0.619	5.28	-7.666	0.606	4.95
MD10	-5.206	0.632	4.676	-5.837	0.605	6.074	-8.629	0.555	5.372	-7.815	0.616	5.386
MD11	-5.43	0.74	4.467	-5.706	0.663	6.003	-6.866	0.614	5.425	-6.069	0.568	4.721
MD12	-3.918	0.756	4.996	-6.182	0.663	5.657	-5.729	0.601	4.963	-9.21	0.624	5.958
MD13	-5.342	0.67	4.289	-5.855	0.586	3.312	-4.296	0.65	4.567	-5.219	0.524	4.611
MD14	-4.055	0.606	4.455	-5.692	0.694	4.833	-5.262	0.647	4.425	-5.213	0.401	4.053
MD15	-4.752	0.653	3.982	-4.443	0.559	5.068	-3.774	0.553	4.154	-4.923	0.464	4.783
MD16	-4.805	0.58	4.293	-5.771	0.717	5.968	-5.127	0.358	4.73	-8.353	0.465	4.96
MD17	-5.327	0.509	5.05	-5.451	0.659	6.332	-4.959	0.361	4.204	-5.276	0.357	4.966
MD18	-5.837	0.684	4.729	-5.365	0.692	6.164	-5.375	0.386	5.019	-5.457	0.455	4.812
MD19	-4.465	0.6	4.19	-5.89	0.636	6.04	-5.755	0.424	4.495	-5.428	0.398	4.249
MD20	-5.214	0.633	4.875	-6.683	0.636	5.478	-4.098	0.46	4.142	-6.47	0.302	4.512
MD21	-4.064	0.731	4.296	-4.842	0.603	4.991	-4.456	0.41	4.448	-6.244	0.273	4.453
MD22	-5.378	0.69	4.653	-5.113	0.591	5.019	-6.053	0.392	4.639	-7.144	0.475	4.802
MD23	-4.677	0.612	4.561	-5.619	0.613	6.064	-5.323	0.528	5.318	-5.077	0.395	4.536
MD24	-4.438	0.587	4.209	-5.878	0.628	5.399	-5.277	0.58	4.548	-4.895	0.471	4.531

CNN Score: convolutional neural network score, CNN Affinity**:** convolutional neural network affinity.

5.3.8.1. Molecular docking of the top scoring hits against Aβ monomer (PDB: 1IYT)

The molecular docking interaction of the compound **MD03** shown in **Figure 5.11A** suggests that it forms hydrophobic interactions with LEU17, VAL18, ALA21, and VAL24 amino acid residues. The docking interaction of the compound MD07 shown in **Figure 5.11B** suggests that there was hydrophobic bond interaction taking place with LEU17, PHE 20, ALA21, VAL24 and MET35 amino acid residues. The π-electrons of the indole group showed π -cation interactions with the LYS16 residue.

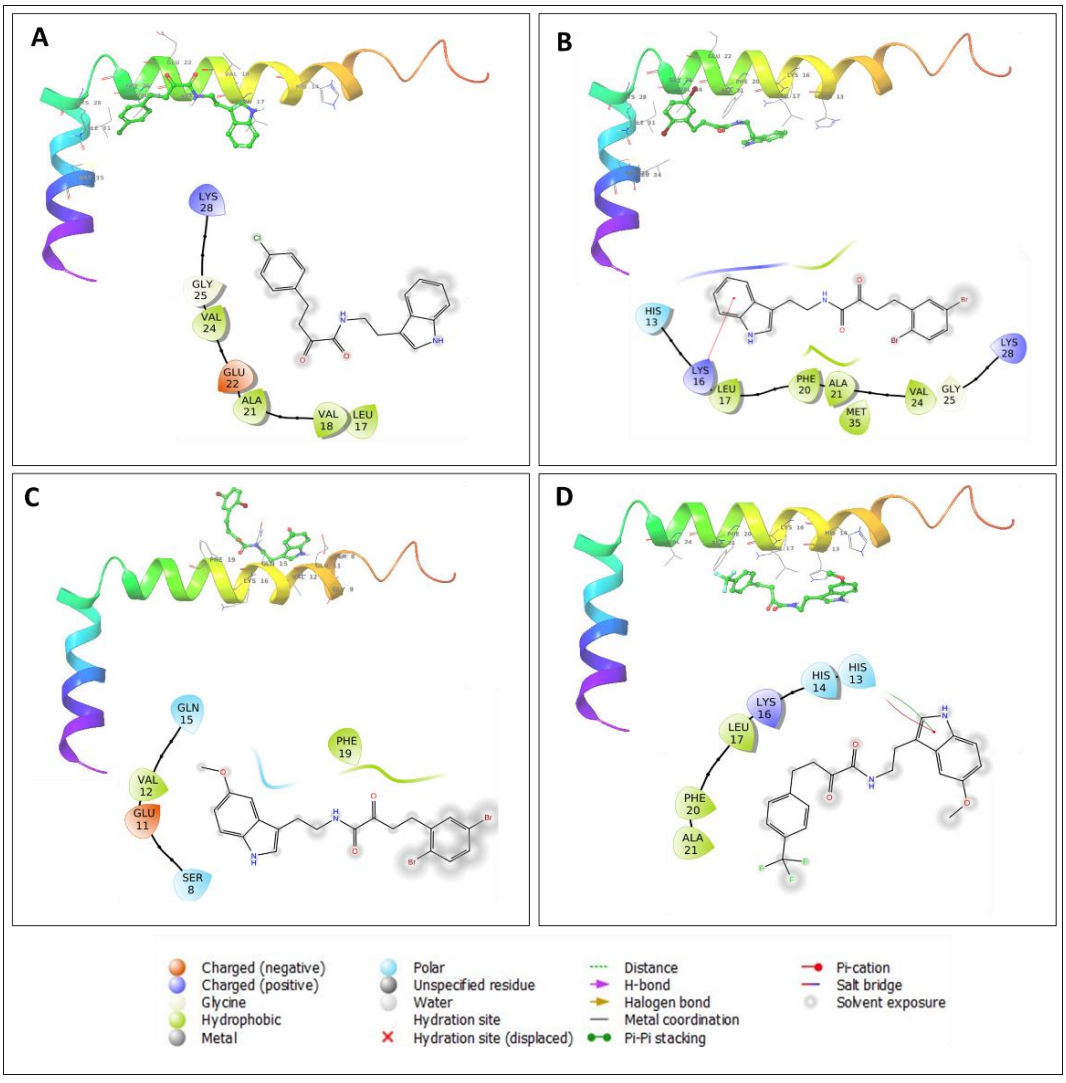

Figure 5.11. The 3D and 2D docking interaction diagram of the top scoring hits MD03 (A), MD07 (B), MD08 (C), MD10 (D) with Aβ monomer (PDB ID: 1IYT).

The interaction diagram for the compound MD08 depicted in **Figure 5.11C** showed that, the indole nucleus is interacting with the VAL12, PHE19 amino acid residues. The docking interaction of the compound MD10 shown in **Figure 5.11D** displayed hydrophobic interactions with the LEU17, PHE20 and ALA21 residues. The π-electrons of the tryptophan ring of the compound MD10 exhibits π-cation as well as π-π stacking with HIS13 residue.

5.3.8.2. Molecular docking study of the tops scoring hits with Aβ pentamer (PDB: 2BEG)

The molecular docking interaction of the compound MD03 shown in **Figure 5.12A** revealed that the compound was interacting in the vicinity of MET_A35, VAL_A36, MET_B35, VAL_B36, MET_C35, VAL_C36, MET_D35, VAL_D36 and MET_E35 residues and the MET_C35 formed a hydrogen bond with the indole moiety.

The molecular docking interaction of the compound MD07 depicted in **Figure 5.12B** revealed that the compound was having hydrophobic interaction with the LEU_A17, VAL_A18, PHE_A19, PHE_A20, ALA_A21, VAL_A36, VAL_A39, VAL_A40 and VAL_B40 amino acid residues. The π-electrons of indole ring also showed π-π stacking with PHE_A20 residue. The α-ketoamide and π-electrons of 2,5-dibromo phenyl group showed H-bond interaction and π-π stacking interaction with the PHE_A19 residue respectively.

The molecular docking interaction of the compound MD08 shown in **Figure 5.12C** revealed that the compound was encased in the hydrophobic pocket formed by the residues ALA_A21, ILE_A32, LEU_A34, VAL_A36, ILE_B32, LEU_B34 and VAL_B36. The carbonyl group of the α-ketoamide also showed H-bond interaction with the ASP_A23 residue.

The molecular docking interaction of the compound MD10 depicted in **Figure 5.12D** revealed that the compound was having hydrophobic interaction with the VAL_A36, VAL_A39, MET_B35, VAL_B36, VAL_B39, MET_C35, VAL_C36, VAL_C39, MET_D35, VAL_D39, MET_E35, VAL_E36 and VAL_E39 amino acid residues and the glycine residues GLY_A37,

GLY_B37, GLY_C37, GLY_D37 and GLY_E37 seems to play an important role in stabilization of the compound MD10 in the Aβ pentamer forming a stable complex.

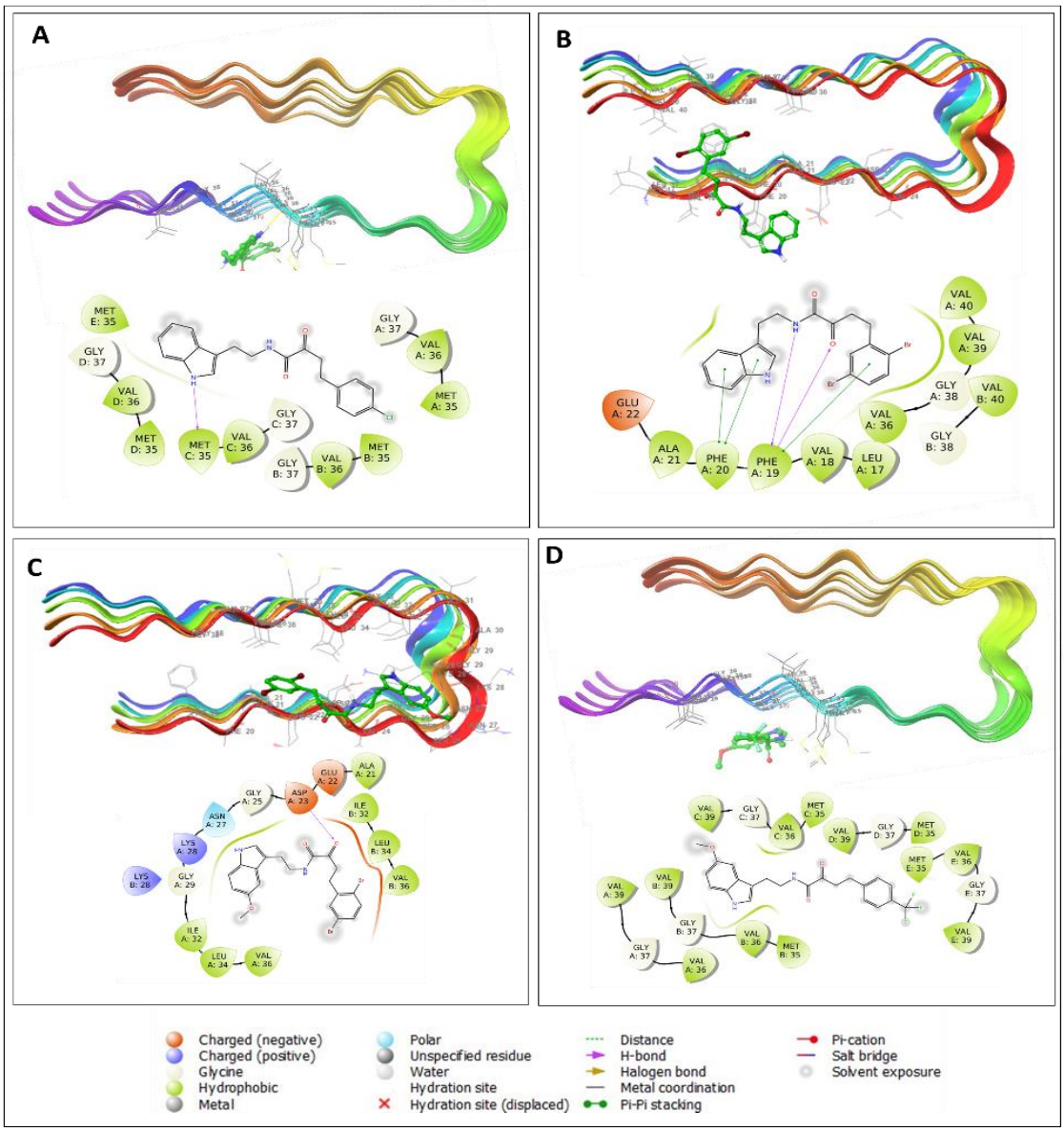

Figure 5.12. The 3D and 2D docking interaction diagram of the top scoring hits MD03 (A), MD07 (B), MD08 (C), MD10 (D) with Aβ pentamer (PDB ID: 2BEG).

5.3.8.3. Molecular docking study of the tops scoring hits with the cluster of tau C6

The docking interaction of the compound MD03 depicted in **Figure 5.13A** indicates that it forms hydrophobic interaction with the ILE297, ILE308, TYR310, VAL313 and PRO364 amino acid residues.

The π-electrons of the indole ring showed π-cation interaction with the LYS298 and LYS317 residues, also the LYS294 and LYS298 formed H-bond with the carbonyl group of the α-ketoamide. The docking interaction of the compound MD07 shown in **Figure 5.13B** suggests that there was hydrophobic interaction with the PRO312, VAL313, LEU315 and LEU325 amino acid residue, the α-ketoamide seems to form H-bond interaction with the VAL313 residue. The docking interaction of the compound MD08 shown in **Figure 5.13C** suggests that there was hydrophobic interaction with the ILE308, PRO363 and PRO364 amino acid residues. The docking interaction of the compound MD10 shown in the **Figure 5.13D** suggests that it shows hydrophobic interactions with the ILE297, ILE308, TYR310, PRO312, VAL313 and PRO364 amino acid residues. LYS298 residue forms H-bond interaction with the carbonyl of the α-ketoamide and π-cation interaction with the indole ring. THE LYS317 also forms π-cation interaction with the indole ring of the MD10.

5.3.8.4. Molecular docking study of the tops scoring hits with the tau monomer cluster 8

The molecular docking interaction of the compound MD03 shown in **Figure 5.14A** indicates hydrophobic interaction with VAL287, ILE308, VAL309, TYR310, PRO312, ILE328, PRO332 and PRO364. The π-electrons of the indole group showed π-π stacking with TYR310 residue and the carbonyl group of the α-ketoamide showed H-bond interaction with TYR310 and LYS311. The π-electrons of the 4-chlorophenyl group also showed π-cation interaction with LYS331. The molecular docking interaction of MD07 shown in **Figure 5.14B** indicates hydrophobic interaction with the ILE297, VAL300, VAL306, ILE308, VAL363 and PRO364 amino acid residues. The carbonyl of the α-ketoamide seems to have H-bond interaction with the HSD299 residue. The docking interaction of the compound MD08 shown in **Figure 5.14C** suggests that there is a hydrophobic bond interaction with the VAL300, VAL306, ILE308, VAL309, TYR310, PRO312, ILE328, PRO332, VAL363 and PRO364 amino acid residues. The amine group of the α-ketoamide formed H-bond interaction with ILE308 residue. The

LYS331 formed π-cation interaction with the π-electrons of 2,5-di-bromo group of the compound MD08.

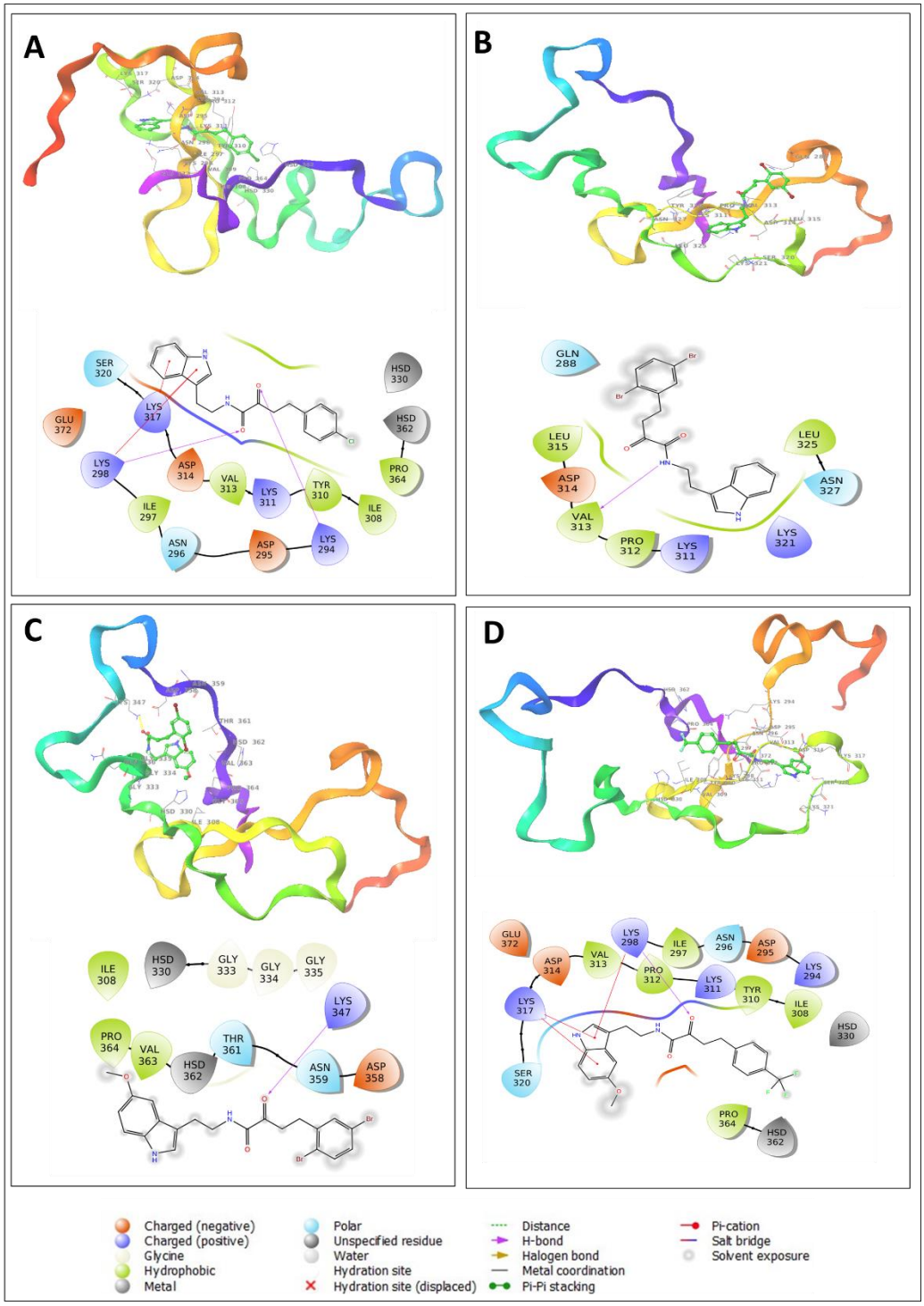

Figure 5.13. The 3D and 2D docking interaction diagram of the top scoring hits MD03 (A), MD07 (B), MD08 (C), MD10 (D) against tau monomer cluster 6.

The docking interactions of the compound MD10 shown in **Figure 5.14D** revealed that it has hydrophobic interaction with the ILE297, VAL300, VAL306, ILE308, TYR310, ILE360, VAL363 and PRO364 amino acid residues, the indoline amine showed H-bond interaction with ILE360 residue.

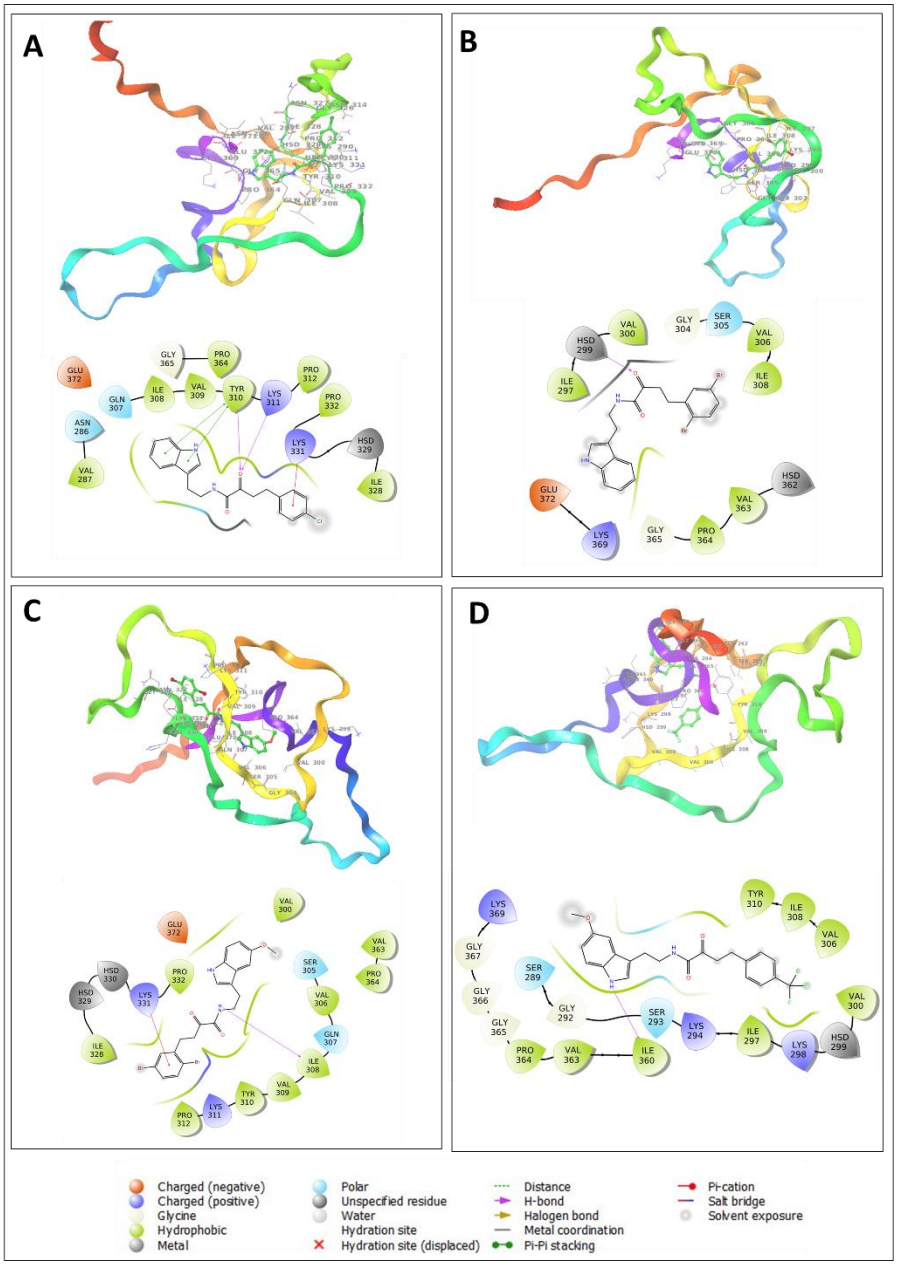

Figure 5.14. The 3D and 2D docking interaction diagram of the top scoring hits MD03 (A), MD07 (B), MD08 (C), MD10 (D) against tau monomer cluster 8.

5.3.9. In Silico Quantum Chemical Studies

5.3.9.1. Optimization of the geometry

The geometrically optimized three-dimensional conformation of the compound MD08 obtained by using the DFT calculation with the help of B3LYP/6-311G (d, p), basis set along with their atomic labelling is represented in **Figure 5.15**. There is a total of forty-nine atoms in the compound.

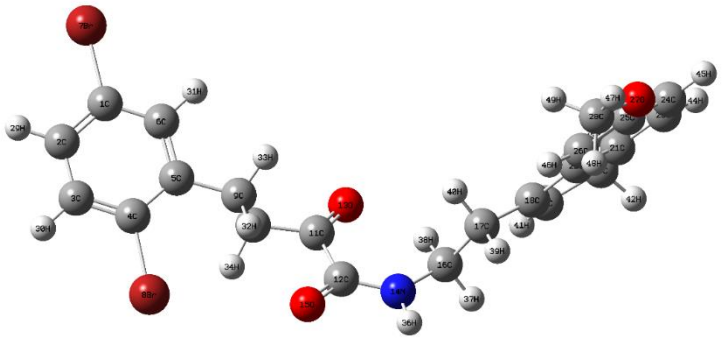

Figure 5.15. Optimized molecular structure by DFT method of lead compound MD08.

5.3.9.2. Molecular Electrostatic potential

Molecular electrostatic potential (MEP) was evaluated for the optimized geometry with the objective of understanding the electrophilic and nucleophilic attack sites available in the molecule. It is a pictorial representation of the electrostatic density in the three-dimensional structural position around the molecule which can help to predict the sites for nucleophilic and electrophilic processes that might occur. Represented with definite colour maps as follows in the ascending order red < orange < yellow < green < blue. The red regions are indicative of negative electrostatic potential having the highest repulsion whereas the positive electrostatic regions are denoted by the blue region having the strongest attraction whereas the green region is for the neutral potential. The regions having the concentrated negative potential in the molecule were identified, the red dots surrounding the 13O and 15O atom on the compound in the MEP map shows the electrophilic reactivity and the region around the carbon atoms represents the nucleophilic reactivity as denoted by the blue colour in the MEP map. The

overall electron density map for the molecular electrostatic potential is shown in **Figure 5.16**.

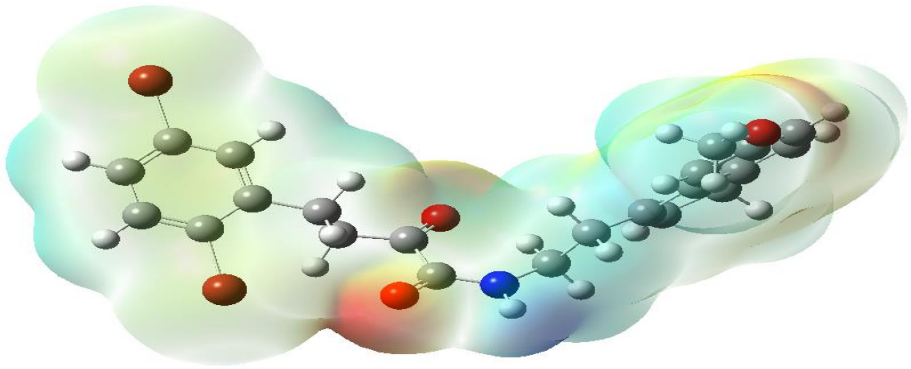

Figure 5.16. Molecular Electrostatic Potential map of lead compound MD08.

5.3.9.3. Frontier Molecular Orbitals (FMOs) analysis

HOMO (Highest Occupied Molecular Orbital) and LUMO (Lowest Unoccupied Molecular Orbital) are concepts in molecular orbital theory that refer to the highest energy electrons in a molecule (in HOMO) and the next available, vacant energy levels (in LUMO). Understanding the energy levels and characteristics of these molecular orbitals can provide insight into a molecule's reactivity, chemical properties, color, and other properties. The energy difference between the HOMO and LUMO, often referred to as the "band gap" in solids, can provide information on a molecule's reactivity. A smaller HOMO-LUMO gap typically results in a molecule being more chemically reactive. The **Figure 5.17** shows the HOMO-LUMO diagram of compound MD08 and the compound appears to be more reactive (E= EHOMO-ELUMO =0.13408 eV) based on the data obtained.

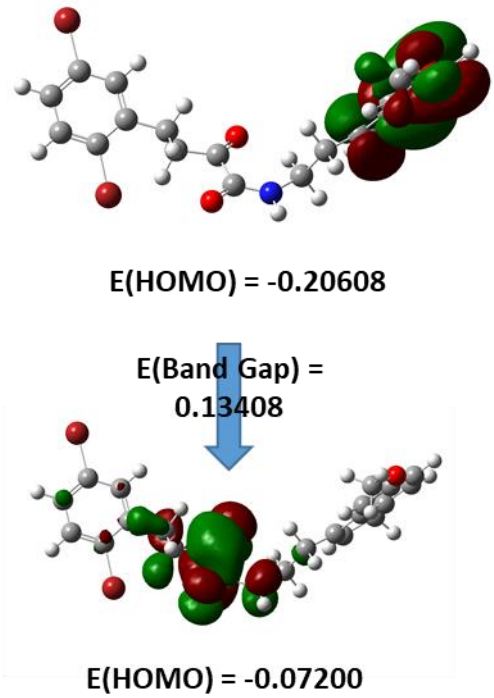

Figure 5.17. The HOMO-LUMO diagram of compound MD08.

5.3.10. Molecular Dynamics Simulation Study

In order to better comprehend the dynamic behavior of the complex of MD08 with Aβ fibril and tau we have performed molecular dynamic simulation for 200ns.

5.3.10.1. Molecular Dynamics Simulation of the MD08-Aβ monomer (1IYT) complex

The radius of gyration (RoG) of the system was evaluated which measures the distribution of the atoms of the protein around the three dimensional space. The RoG value quantifies how much the atoms are spread out from the center of the mass of molecule. Thus, providing us with an insight into the overall size and compactness of the biomolecules, enabling us to study the structural transitions, protein folding, aggregation, and other conformational changes that might occur during the MD simulation. RoG value of the complex MD08 with Aβ (1IYT) is depicted in (**Figure 5.18A**)

A relatively high RoG value of 1.8 nm was observed at the beginning of the simulation and it stabilized in the first 10 ns of the simulation and was then observed within the range of 1.1-1.3

nm which explains that the system is relatively stable and is constantly evolving its three-dimensional structure in order to form a stable complex. There was no abnormality observed during the simulation time period of 200 ns. Furthermore, the root mean square deviation (RMSD) of the simulated system was evaluated (**Figure 5.18B**) in order to understand the overall stability of the simulated system, as it measures the difference between the backbone of the protein from its initial position at the starting of the simulation to the final conformation obtained after the simulation.

The RMSD plot for the Aβ (1IYT) protein in the simulated complex depicted in (**Figure 5.18B**) in blue color was seen to be in the range of 0.5-1.2 nm showing that it reached convergence, but the higher RMSD value was due to the fact that Aβ (1IYT) is a small peptide of 42 amino acid residues thus making it more flexible. Likewise, the RMSD plot for the compound MD08 shown in (**Figure 5.18B**) in purple color seems to be in the range of 0.75-2 nm, where the minor fluctuations are due to the small size of the compound which is constantly rearranging in the binding site with the Aβ in order to form a stable complex and reach its global energy minima. Root Mean Square Fluctuation (RMSF) is a commonly used analysis in MD simulations to analyze the flexibility and stability of biomolecules. It provides information about the dynamic behavior of individual atoms or groups of atoms throughout the simulation. RMSF analysis provides insights into the crucial amino acid residues that are responsible for the dynamic behavior of biomolecules and can be used to study conformational changes, protein-ligand interactions occurring during an MD simulation. The RMSF of the compound MD08 (**Figure 5.18C**) seems to be in the range of 0.1 to 0.46 nm which explains the flexibility of the compound as a small molecule that allows it to interact with the various amino acids of the Aβ monomer in order to form a stable complex. The RMSF of the Aβ (1IYT) protein (**Figure 5.18D**) have been found to fluctuate in between the range of 0. 1 to 1.25 nm that indicates the flexibility of the protein throughout the simulation period.

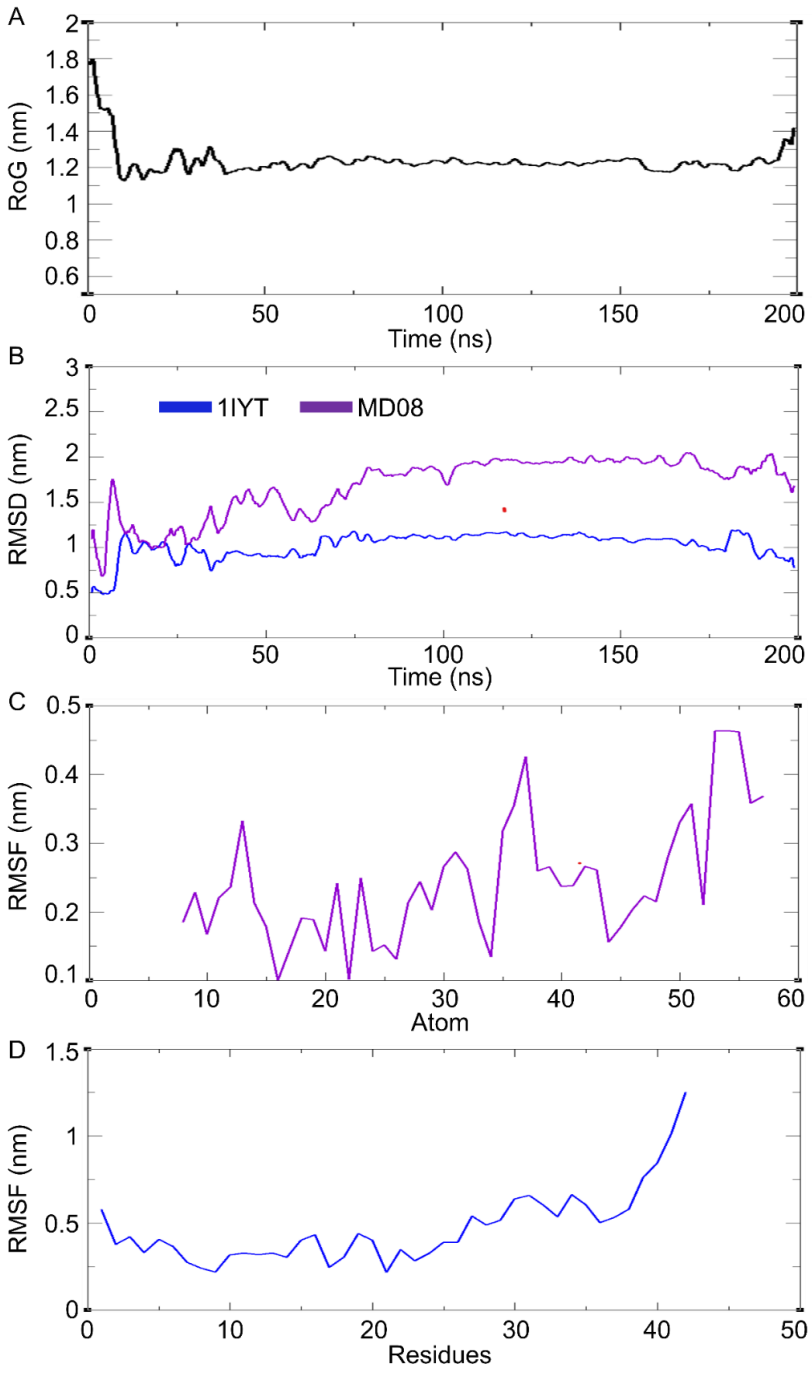

Figure 5.18. Molecular dynamics trajectory analysis of MD08-Aβ monomer complex. (A) RoG, (B) RMSD, (C) RMSF of ligand (D) RMSF of protein.

In order to better understand key interaction between the protein ligand interaction that might help in the stabilization of the formed complex, the number of hydrogen bonds formed during the MD simulation was analyzed. In general, the optimal distance for a hydrogen bond donor and acceptor is ≤3.5 Å (0.35 nm) with an angle of 180° ± 30°. Here we have investigated the

average number of H-bond formation during the 200 ns simulation with the cut-off value set at 0.35 nm (**Figure 5.19A**). It can be clearly observed that the formed complex maintains about 2-5 H-bond between MD08 and Aβ (1IYT) protein throughout the 200 ns of the simulation. Hydrogen bond distance (HBD) shown in (**Figure 5.19B**) can be noticed that the average H-bond distance was maintained at about 0.3 nm.

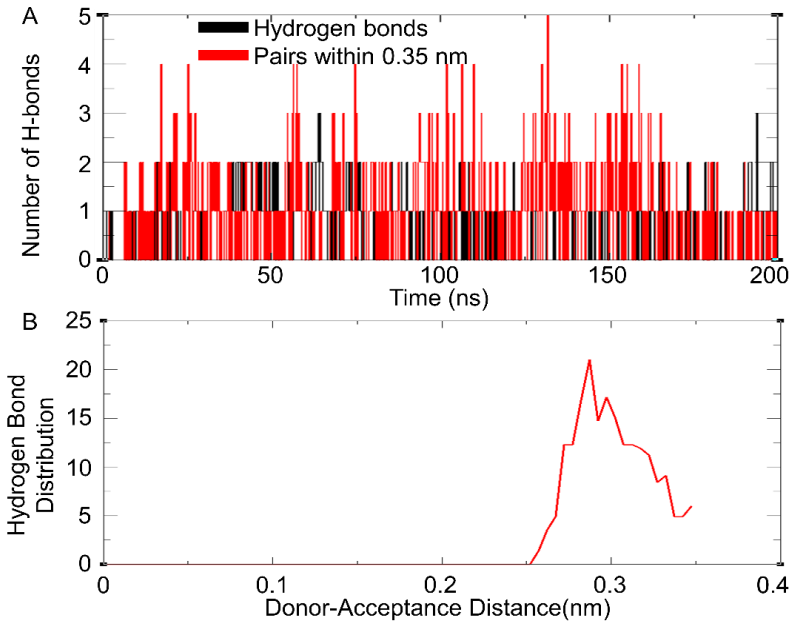

Figure 5.19. **Hydrogen bond analysis of MD08-Aβ monomer complex MD trajectory**. (A) Total number of H-bonds, and (B) Hydrogen bond distribution.

5.3.10.2. Molecular dynamics study of complex MD08 with pentamer 2BEG

Likewise, for the MD08 with the pentamer of Aβ (PDB:2BEG). The RoG value of the complex MD08 with pentamer of Aβ (PDB:2BEG) is depicted in (**Figure 5.20A**). A relatively high but stable RoG value within the range of 1.39-1.42 nm was observed as expected due to the small peptide nature of the protein having good flexibility and was constantly evolving with respect to its three dimensional structure during the complex formation and abnormality was observed during the 200 ns simulation. Furthermore, the RMSD of the simulated system was evaluated shown in (**Figure 5.20B**), where the RMSD for the Aβ pentamer (2BEG) protein shown in blue colour seems to be in the range of 0.5-0.75 nm which seems to be stable during the simulation

without any abrupt changes. Likewise, The RMSD plot for the compound MD08 shown in (**Figure 5.20B**) purple colour was in the range of 0.6-1 nm, which seems to be stable. The RMSF plot for compound MD08 shown in (**Figure 5.20C**) have been found to be in between 0.05-0.3 nm that indicates the flexibility of the ligand throughout the simulation period that helps it to change its geometric orientation in order to make a complex with the Aβ pentamer in order to form a stable complex and reach energy minima.

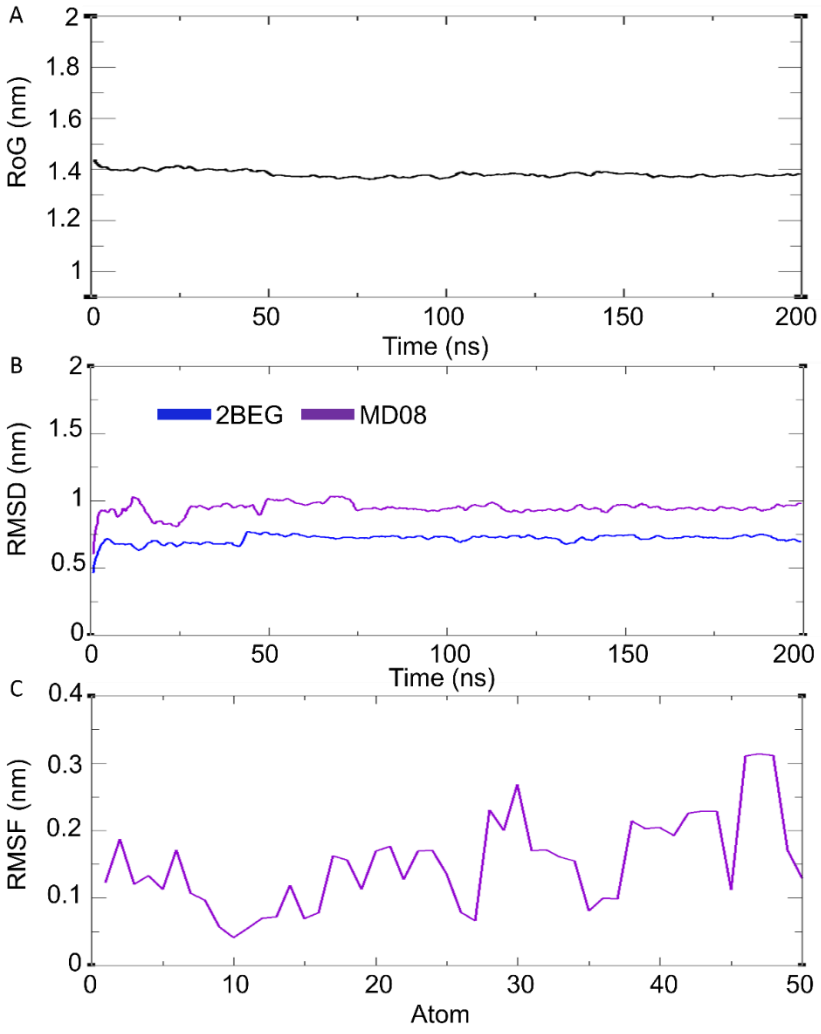

Figure 5.20. Molecular dynamics trajectory analysis of MD08-Aβ pentamer complex. (A) RoG (B)RMSD. (C) RMSF of ligand.

Likewise, the average number of H-bond formation during the 200 ns simulation with the cut-off value set at 0.35 nm was evaluated for the compound MD208 with the pentamer of Aβ

(PDB:2BEG) (**Figure 5.21A**). There seems to be several instances where there is no H-bond formation between MD08 and pentamer of Aβ (PDB:2BEG) during the first 50 ns time interval of the simulation, followed by an average of 1-2 H-bond formation for the remaining time span in between. Hydrogen bond distance (HBD) shown in (**Figure 5.21B**) it can be noticed that the average H-bond distance was about 0.3 nm.

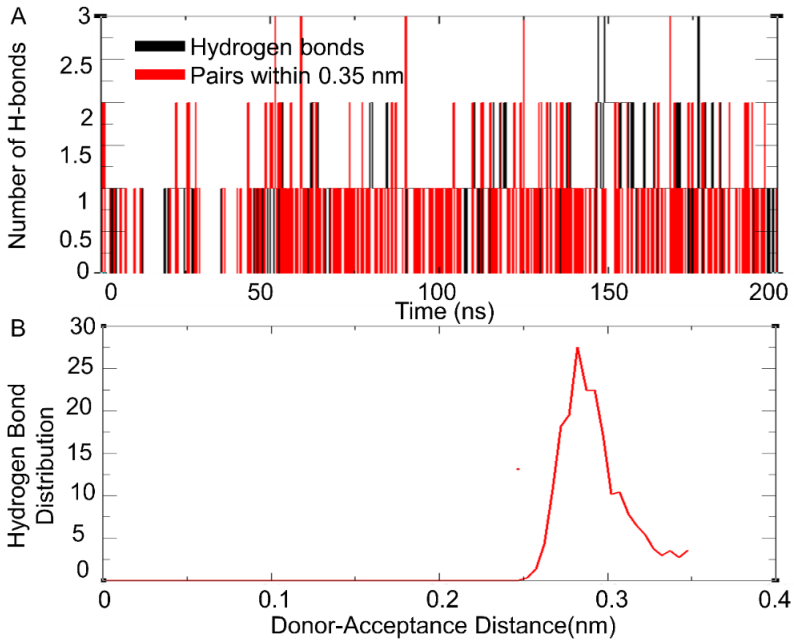

Figure 5.21. Hydrogen bond analysis of MD08-Aβ pentamer complex MD trajectory. (A) Total number of H-bonds, and (B) Hydrogen bond distribution**.**

5.3.10.3. Molecular dynamics study of complex MD08 with tau cluster 06 (C06)

We have also performed the simulation of the compound MDO8 with the top scoring cluster C06 of tau protein. The evaluated parameters are shown in (**Figure 5.22**). The RoG value of the complex MD08 with CO6 is shown in (**Figure 5.22A**). A relatively high RoG value in the range of 1.5-2.25 nm was observed as expected due to the small size of the tau protein and having good flexibility and was constantly evolving during the complex formation as it belongs to the intrinsically disordered proteins. However, there was no uncertain motion observed during the simulation time frame. Furthermore, the RMSD of the simulated system was

evaluated (**Figure 5.22B**), where the RMSD C06 protein shown in blue colour seems to be in the range of 0.75-1.75 nm which seems to be fluctuating throughout the simulation and was unstable past 100 ns of the simulation, which denotes that the complex formation was taking place however the system was not very stable. Likewise, the RMSD plot for the compound MDO8 shown in (**Figure 5.22B**) purple colour was in the range of 0.5-1.25 nm, which seems to be stable having some fluctuations during the simulation due to the flexible nature of the compound which results in constant adjustment in the binding process with the C06 tau protein in order to reach energy minima.

The RMSF plot for compound MD08 shown in (**Figure 5.22C**) have been found to be in between 0.1-0.45 nm that indicates the flexibility of the ligand throughout the simulation period which helps it to rearrange in order to make a complex with the tau protein in order to form a stable complex and reach energy minima. Furthermore, the C06 tau protein RMSF depicted in (**Figure 5.22D**) was observed in the range of 0.5-2.25 nm which is due to the nature of the tau protein as it belongs to the intrinsically disordered proteins and is a small protein system.

The average number of H-bond formation during the 200 ns simulation with the cut-off value set at 0.35 nm was calculated for the complex MD08 with the C06 tau protein cluster (**Figure 5.23A**). It can be noticed that it maintained 1-4 H-bond formation between MD08 and C6 on an average throughout the time interval of the simulation Hydrogen bond distance (HBD) shown in (**Figure 5.23B**) it can be seen that the average H-bond distance was maintained about 0.3 nm.

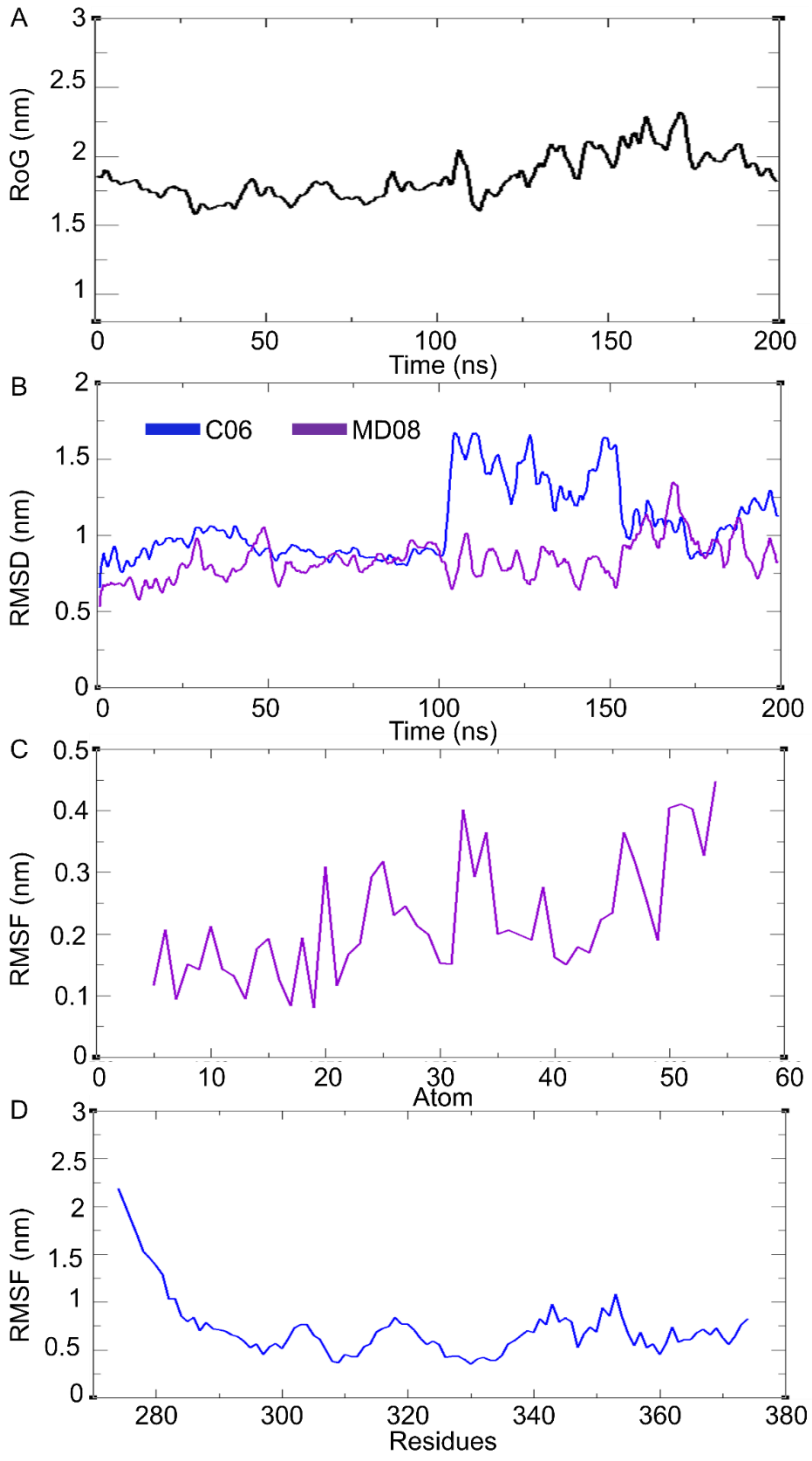

Figure 5.22. Molecular dynamics trajectory analysis of MD08-tau monomer cluster 6 complex. (A) RoG (B) RMSD (C) RMSF (D) RMSF of protein.

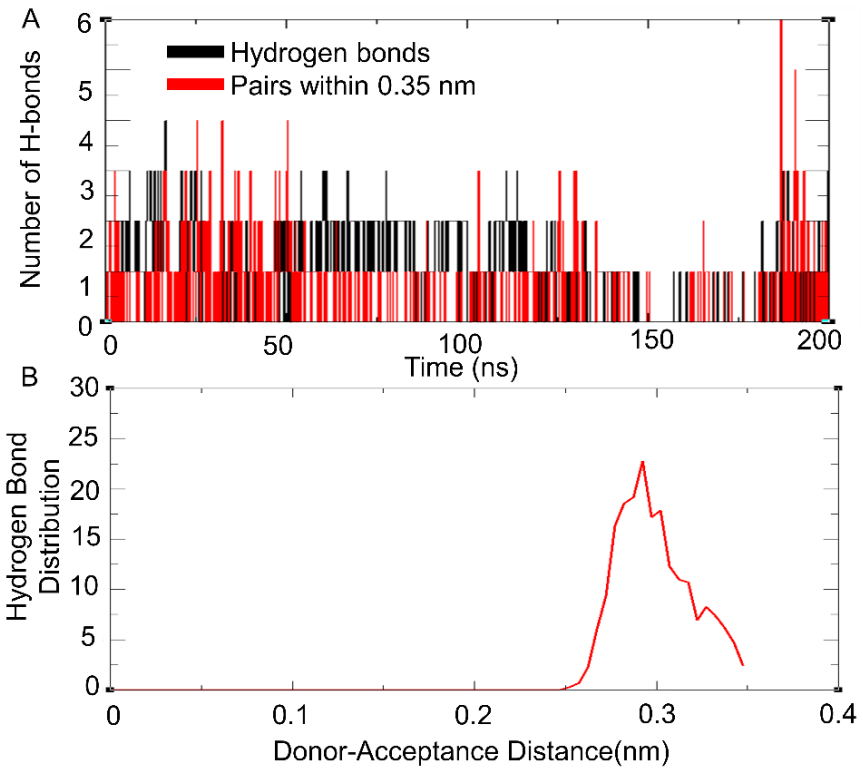

Figure 5.23. Hydrogen bond analysis of the MD08-tau monomer cluster 6 complex. (A) Total number of H-bonds, and (B) Hydrogen bond distribution.

5.3.10.4. Molecular dynamics study of complex MD08 with tau cluster 8 (C08)

Likewise, the simulation for the compound MD08 with the top scoring cluster C08 of tau protein was also carried out and evaluated (**Figure 5.24**). The RoG value of the complex MD08 with C08 is depicted in (**Figure 5.24A**) and was observed in the range of 1.5-2.5 nm, where it can be seen from the graph that there is a shift in RoG value during the first 150 ns of the simulation and then seems to stabilize at 1.5 nm. There was no uncertainty observed during simulation time frame. Furthermore, the RMSD of the simulated system is shown in (**Figure 5.24B**), where the RMSD C08 protein represented in blue colour on the graph seems to be in the range of 0.5-2 nm which seems to be slightly fluctuating during the first 150 ns then reached convergence and seems to be stable at 1.5 nm which denotes that the complex formation was taking place. Likewise, The RMSD plot for the compound MD08 shown in (**Figure 5.24B**) purple colour was in the range of 0.5-1.25 nm, which seems to be relatively stable having minor

fluctuations due to the flexible nature of the compound which results in constant adjustment in the binding process with the C08 tau protein in order to reach energy minima.

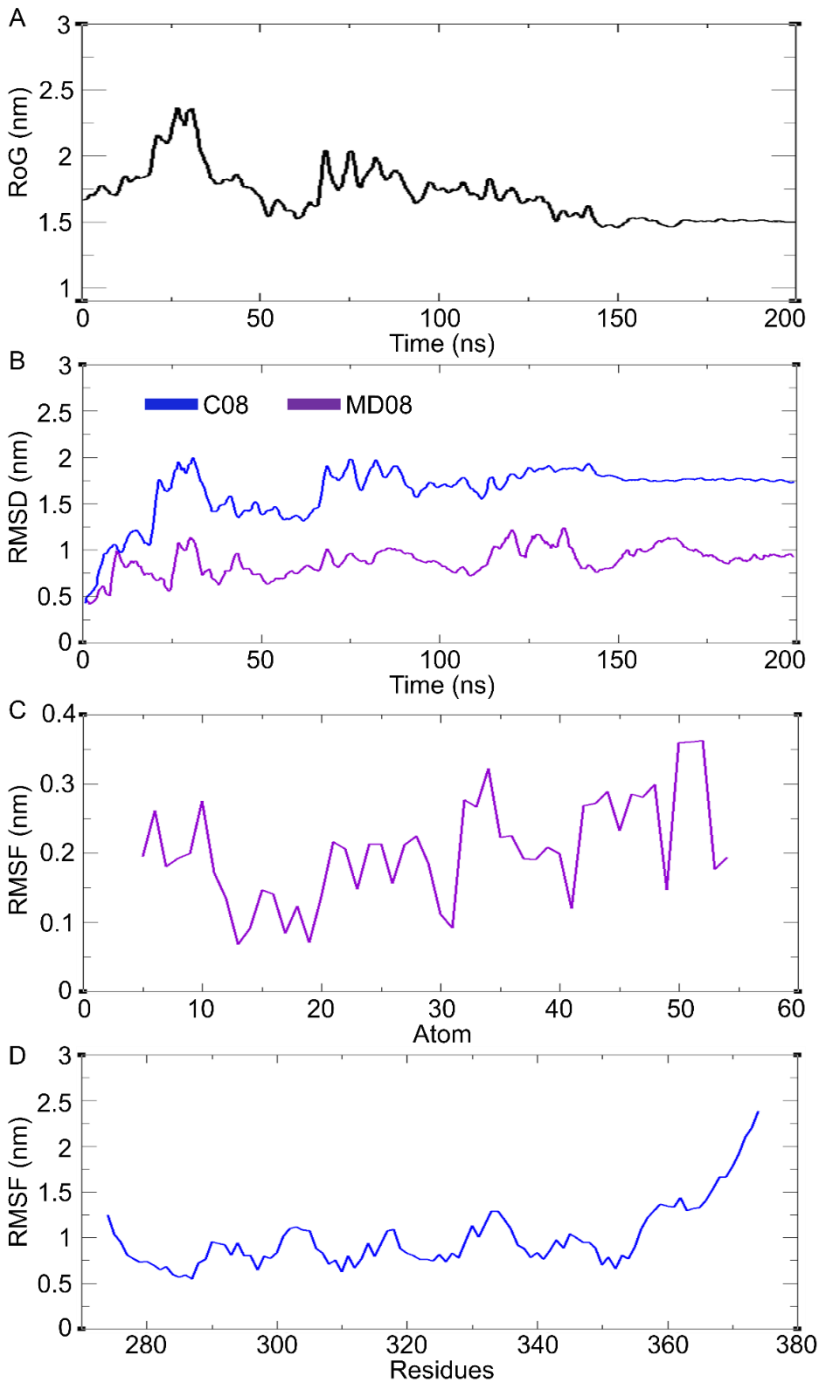

Figure 5.24. **Molecular dynamics trajectory analysis of MD08-tau monomer cluster 8 complex.** (A) RoG (B) RMSD, (C) RMSF of ligand, (D) RMSF of protein.

The RMSF plot for compound MD08 shown in (**Figure 5.24C**) was observed in the range of

0.05-0.35 nm that indicates the flexibility of the ligand throughout the simulation period which helps it to rearrange in order to make a complex with the tau protein in order to form a stable complex and reach energy minima. Furthermore, the C08 tau protein RMSF depicted in (**Figure 5.24D**) was observed in the range of 0.5-2.25 nm which bit high due to the flexibility of the protein.

The average number of H-bond formation during the 200 ns simulation with the cut-off value set at 0.35 nm was estimated for the complex MD08 with the C08 tau protein cluster (**Figure 5.25A**). It can be observed that on an average it maintained 2-5 H-bond formation between MD08 and C08 throughout the simulation time. Hydrogen bond distance (HBD) shown in (**Figure 5.25B**) it can be seen that the average H-bond distance was maintained about 0.3 nm.

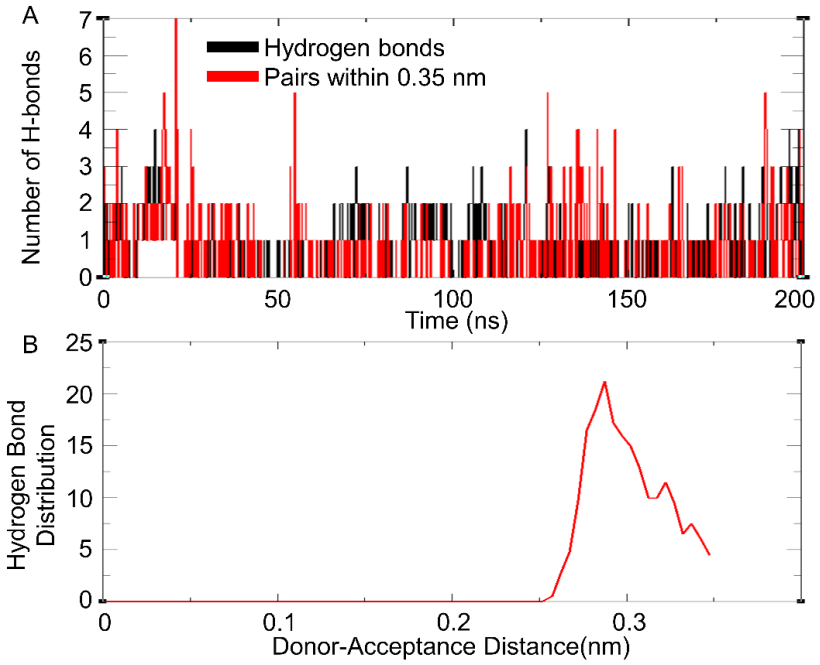

Figure 5.25. Hydrogen bond analysis of the compound MD08-tau monomer cluster 8 complex. (A) Total number of H-bonds, and (B) Hydrogen bond distribution.

5.3.10.5. Principal component analysis (PCA)

Principal Component Analysis (PCA) in the context of molecular dynamics (MD) simulations is a popular method to identify and characterize the collective motions of atoms or molecules.

This technique is commonly termed "essential dynamics. It identifies dominant modes of motion in a protein or biomolecule, which are often related to its function. Reduce the dimensionality of an MD trajectory for easier analysis and visualization. We have performed the principal component analysis (PCA) for all the simulated system complexes. The eigenvalues of the first 10 principal components (eigenvectors) for MD08 with various Aβ and tau complexes are shown in **(Figure 5.26).**

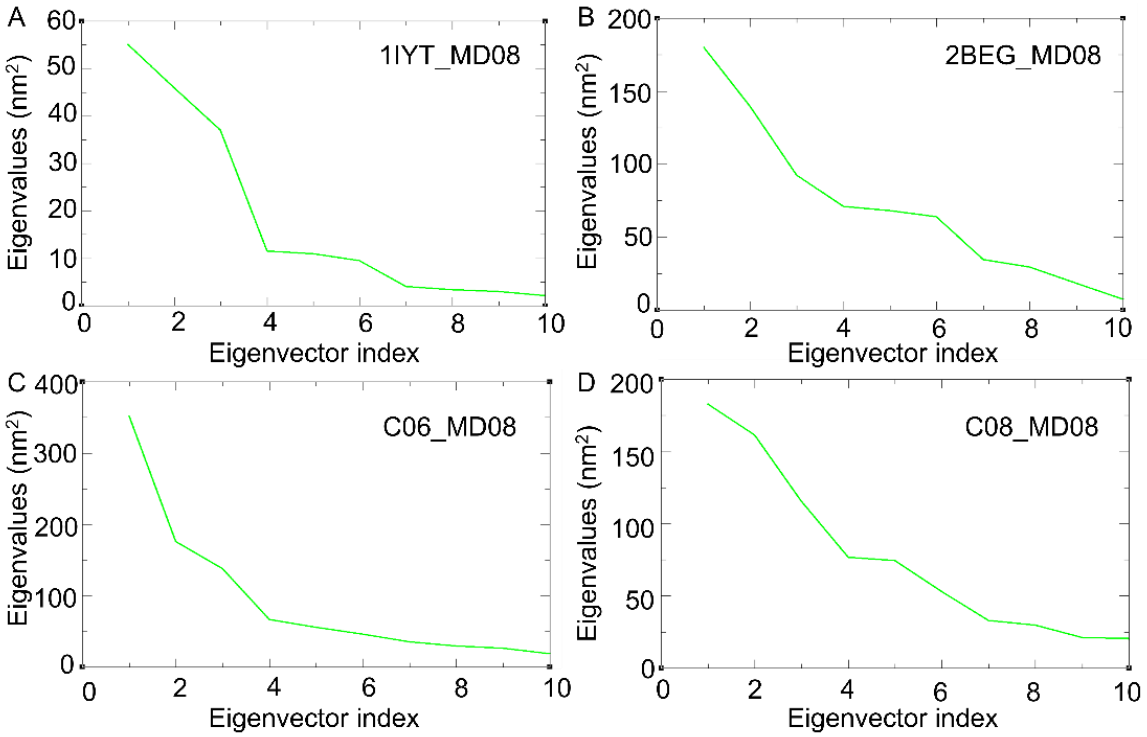

Figure 5.26. Eigenvalues of the first principal components of the simulated system for the Aβ and tau cluster with the compound MD08. (A) Eigenvalues of the first principal components of the simulated system for the MD08-Aβ monomer complex (B) Eigenvalues of the first principal components of the simulated system for the MD08-Aβ pentamer complex (C) Eigenvalues of the first principal components of the simulated system for the MD-C06 tau complex (D) Eigenvalues of the first principal components of the simulated system for the MD08-C06 tau complex. Here, the principal component analysis identifies the most contributing parameters that explain the structural stability of Aβ and tau complex during its

interaction with the MD08.

These analyses showed that the first two components explained most of the variations in the data and then the graph slowly declines and becomes horizontal having the least explain ability. Finally, we used the first two principal components to plot the 2D PCA plot (**Figure 5.27**). The PCA graph denotes the various conformational changes that occurred during the complex formation. The 2D plot shows concentrated distribution in the conformational space with stable clusters for the MD08 complexed with the monomer and pentamer of Aβ protein, most likely due to various conformational changes in the protein structure upon molecular interaction with the compound MD08, resulting in various stable conformational states. Likewise, for the complex of MD08 with the clusters 06 and cluster 08 of tau it can be observed a widespread distribution which might be due to some minor uncertainties during the folding process during the course of simulation.

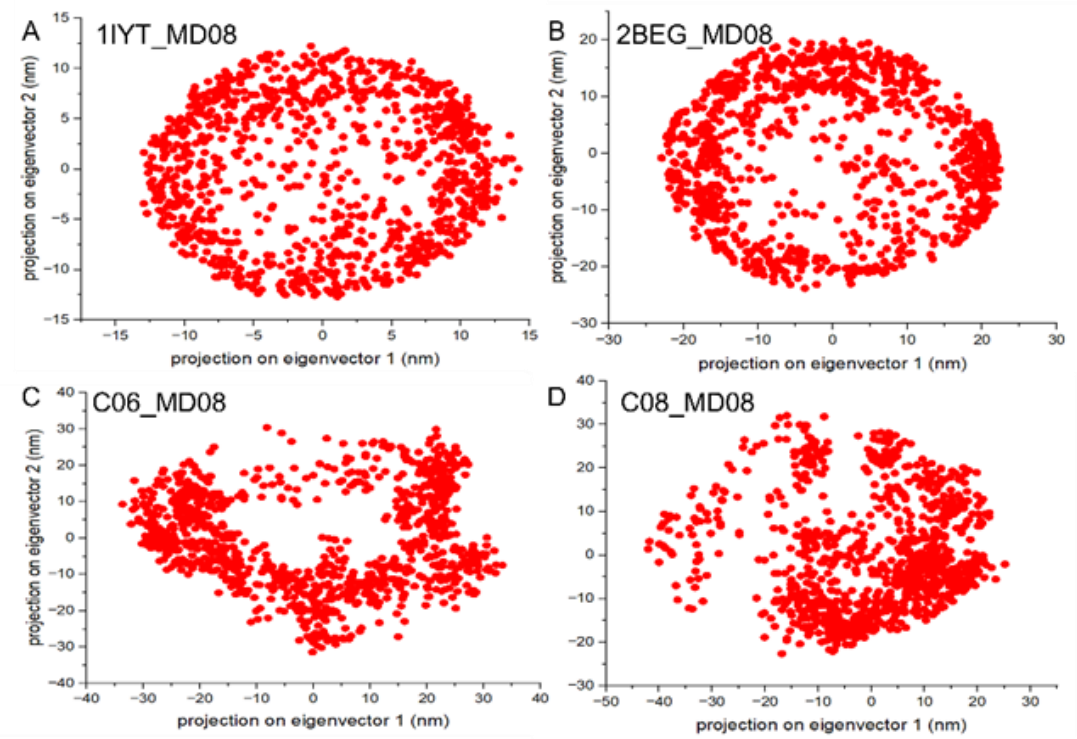

Figure 5.27. The 2D projection of the first two principal components for the MD08-Aβ monomer complex (A), MD08-Aβ pentamer complex (B), MD08-C06 tau complex

(C), and MD08-C08 tau complex. Each dot on the plot is representation of a specific conformational state in the different Aβ and tau proteins with the ligand MD08 throughout the simulation. The spread represents the primary conformational changes in the Aβ and tau protein during the interaction of MD08 during the simulation.

5.3.11. Free energy landscape analysis (FEL)

Free energy landscape (FEL) analysis in molecular dynamics (MD) simulations is a powerful technique used to understand the thermodynamic and kinetic properties of complex molecular systems. FEL can be representative of two variables that can directly reflect the distinctive properties of the system and measure the conformational changes. The Free Energy Landscape (FEL) serves as an indicator for two crucial factors that highlight the unique characteristics of the system and track alterations in its conformation. To map out the free energy minimum landscape for our complexes, we evaluated the FEL in the context to the RoG and RMSD as the two primary reaction coordinates, as depicted in (**Figure 5.28**). An in-depth look at the energy landscape allowed us to discern its shape and dimensions. Here, small, centralized blue regions suggest a complex within the cluster exhibiting maximum stability and shows that the system has converged to its energy minima conformation. The slender funnel visible in the 3D visualizations signifies the dynamic conformational shifts over time, driving the system towards adopting a native structure at its energy optimum. The overall 3D plots revealed that the complex of MD08 with monomer and pentamer of Aβ shows the lowest energy minima in the form of less number of funnels in comparison to a complex of MD08 with two different clusters of tau suggesting that the stability of other complex.

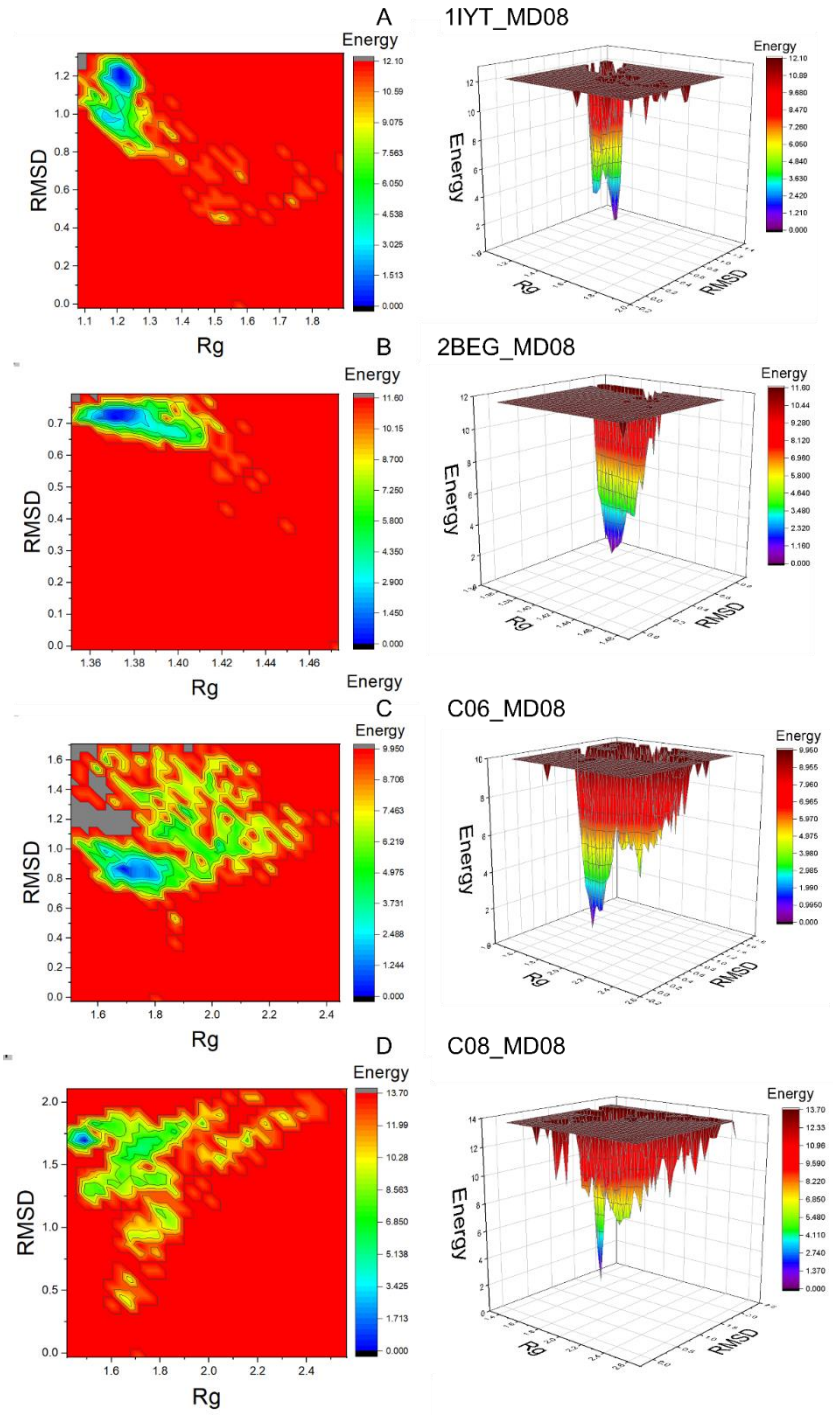

Figure 5.28. The 2D and 3D free energy landscape diagram as a function of RMSD and RoG as the two coordinates of the Aβ and tau complex with MD08. The free energy is displayed in terms of kj/mol where the purple Colour indicates the least energy and red the highest energy. The folding funnel formed by the complex MD08 with Aβ monomer, Pentamer, cluster06 of tau, and cluster 08 of tau shows stable folding. The complex MD08 showed less

number of funnel in monomer and pentamer of Aβ than tau suggesting stability of the complex.

5.3.12. In silico ADME analysis

For optimal bioavailability of a molecule, it is crucial that the molecule demonstrates both excellent solubility and desirable pharmacokinetic characteristics. In line with this, we analyzed the pharmacokinetic properties of twenty-four compounds, leveraging the capabilities of the Swiss ADME web server discussed in the **Chapter 4, Section 4.3.12**.

Table 5.6 comprehensively enumerates the pharmacokinetic features of these compounds, abiding by the Rule of Five parameters: molecular weight (MW), lipophilicity (iLOGP), hydrogen bond acceptors (HBA), and hydrogen bond donors (HBD). Additionally, ancillary parameters like the total polar surface area (TPSA) and the number of rotatable bonds are also presented for a holistic understanding. A perusal of the molecular weights of the series (compounds MD01 through MD24) reveals a range spanning from 320.39 to 525.19 g/mol. A predominant portion of these compounds exhibited commendable attributes, such as an average number of rotatable bonds, and numbers of H-bond acceptors and donors that align with optimal drug properties. Predominantly, the compounds conform to Lipinski's Rule of Five – a quintessential rubric for anticipating the "drug-likeness" based on select physicochemical properties. Nevertheless, deviations were noted for compounds MD13, MD16, MD17, MD18, and MD19. These particular compounds registered PAINs alerts with a value of 1, indicating potential assay interference.

Table No 5.6. ADME properties of the synthesized compounds calculated using Swiss ADME webserver.

Compound	MW	Rotatable bonds	H-bond acceptor	H-bond donors	MR	TPSA	LOGP	Bioavailability Score	PAINS alerts	BBB Permeability
MD01	320.39	8	2	2	94.99	61.96	2.27	0.55	0	Yes
MD02	350.41	9	3	2	101.48	71.19	2.4	0.55	0	Yes
MD03	354.83	8	2	2	100	61.96	2.47	0.55	0	Yes
MD04	384.86	9	3	2	106.49	71.19	2.74	0.55	0	Yes
MD05	338.38	8	3	2	94.95	61.96	2.34	0.55	0	Yes
MD06	368.4	9	4	2	101.44	71.19	2.53	0.55	0	Yes
MD07	478.18	8	2	2	110.39	61.96	2.71	0.55	0	Yes
MD08	508.2	9	3	2	116.88	71.19	3.17	0.55	0	Yes
MD09	388.38	9	5	2	99.99	61.96	2.2	0.55	0	Yes
MD10	418.41	10	6	2	106.48	71.19	2.75	0.55	0	No
MD11	365.38	9	4	2	103.81	107.78	1.71	0.55	0	No
MD12	395.41	10	5	2	110.3	117.01	2.09	0.55	0	No
MD13	367.4	7	4	0	110.83	86.44	2.35	0.55	1	No
MD14	350.45	6	2	0	111.94	40.62	3.41	0.55	0	Yes
MD15	347.41	6	3	0	106.72	64.41	2.78	0.55	0	Yes
MD16	401.84	7	4	0	115.84	86.44	2.22	0.55	1	No
MD17	525.19	7	4	0	126.23	86.44	2.63	0.55	1	No
MD18	435.4	8	7	0	115.83	86.44	2.48	0.55	1	No
MD19	385.39	7	5	0	110.79	86.44	2.61	0.55	1	No
MD20	368.44	6	3	0	111.9	40.62	3.66	0.55	0	Yes
MD21	365.4	6	4	0	106.68	64.41	2.9	0.55	0	Yes
MD22	412.4	8	6	0	119.65	132.26	2.42	0.55	1	No
MD23	395.45	7	4	0	120.76	86.44	3.12	0.55	0	No
MD24	392.41	7	5	0	115.55	110.23	2.5	0.55	0	No

MW: molecular weight; MR: molecular refractivity; TPSA: topological polar surface area; ILOGP, XLOGP3, WLOGP, and MLOGP are the predictive models of Swiss ADME and their values indicate lipophilicity of molecules.

5.4. Material Methods

5.4.1. Chemistry

All the reagents and chemicals used for the synthesis and characterization of compounds were purchased from Sigma-Aldrich, Alfa-Aesar, and SRL (Sisco Research Laboratories Pvt. ltd). The solvents were dried by standard solvent drying methods. The compounds were characterized by AVH D 500 AVANCE III HD 500 MHz OneBay NMR Spectrometer at IITBHU, and High-resolution mass spectra (HRMS) were obtained by electrospray (HRMS/ESI), recorded with Agilent1100 LC-Q-TOF and HRMS-6540-UHD machine at Department of Chemistry, Banaras Hindu University. All the structures were drawn by using ChemDraw Professional 16. For sample quantification, we used RP-HPLC Agilent 1260 infinity II**.** The NMR, Mass spectrum of all compounds and HPLC calibration curve & perecentage purity data of MD08 is given in **Annexure II (320-357).**

5.4.1.1. General Procedure for the synthesis of compound MD01 to MD24

The procedure for the synthesis of starting material **β,γ-unsaturated α-hydroxy thioesters** (**4a-f**) has been well discussed in the **Chapter 4, Section 4.4.1.1**. Then *β,γ*-Unsaturated *α*-hydroxy thioesters*:* **4a-f** (0.05 g, 1.0 equiv) was dissolved in dry dichloromethane (DCM) (1.0 mL), and the respective amine (3.0 equiv) was added to the reaction mixture. The reaction mixture was allowed to stir at room temperature for 20- 30 min. After completion of the reaction, water was added, and the product was extracted with DCM. The combined organic layers were dried over anhydrous Na_2SO_4 and filtered, and the filtrate was concentrated under reduced pressure to get a residue. The crude residue was purified over silica gel column chromatography [100−200], eluent: ethyl acetate/n-hexane] to obtain the pure product.

5.4.1.1.1. N-(2-(1H-indol-3-yl)ethyl)-2-oxo-4-phenylbutanamide **(MD-01)**

Yellow solid, 75 % yield. **^{1}H NMR (500 MHz, $CDCl_3$): δ** 8.08 (s, 1H), 7.62 (d, *J* = 7.9 Hz, 1H), 7.40 (d, *J* = 8.1 Hz, 1H), 7.31 (d, *J* = 7.5 Hz, 3H), 7.24 (dd, *J* = 14.9, 7.8 Hz, 3H), 7.16 (t, *J* = 7.5 Hz, 1H), 7.05 (s, 2H), 3.66 (q, *J* = 6.7 Hz, 2H), 3.29 (t, *J* = 7.5 Hz, 2H), 3.04 (t, *J* = 6.9 Hz, 2H), 2.95 (t, *J* = 7.5 Hz, 2H). **^{13}C NMR (126 MHz, $CDCl_3$): δ** 198.26, 160.00, 140.41, 136.44, 128.44 (d, *J* = 16.4 Hz), 127.12, 126.25, 122.36, 122.03, 119.62, 118.64, 112.46, 111.30, 39.47 , 38.30, 29.72, 29.14, 25.14. **HRMS (ESI):** m/z calculated for $C_{20}H_{20}N_2O_2$ $[M+H]^+$: 321.1603; found : 321.1601

5.4.1.1.2. N-(2-(5-methoxy-1H-indol-3-yl)ethyl)-2-oxo-4-phenylbutanamide **(MD-02)**

Yellow solid, 77% yield. **^{1}H NMR (500 MHz, $CDCl_3$): δ** 7.99 (s, 1H), 7.33 – 7.23 (m, 3H), 7.14 (d, *J* = 8.5 Hz, 2H), 7.03 (dd, *J* = 7.4, 2.3 Hz, 3H), 6.90 (dd, *J* = 8.8, 2.5 Hz, 1H), 3.88 (s, 3H), 3.64 (dd, *J* = 13.1, 6.8 Hz, 2H), 3.26 (t, *J* = 7.4 Hz, 2H), 3.00 (t, *J* = 6.8 Hz, 2H), 2.90 (t, *J* = 7.4 Hz, 2H). **^{13}C NMR (126 MHz, $CDCl_3$): δ** 197.98, 159.91, 154.19, 138.84, 132.02, 131.56, 129.76, 129.3, 129.16, 128.66, 127.52, 122.80, 112.60, 112.09, 100.46, 55.95, 44.62, 42.79, 39.43, 38.11, 29.71, 28.46, 25.08, 14.16. **HRMS (ESI):** m/z calculated for $C_{21}H_{22}N_2O_3$, $[M+H]^+$: 351.1709; found 351.1702

5.4.1.1.3. N-(2-(1H-indol-3-yl)ethyl)-4-(4-chlorophenyl)-2-oxobutanamide **(MD03)**

White solid, 87 % yield, **^{1}H NMR (500 MHz, $CDCl_3$): δ** 8.08 (s, 1H), 7.61 (d, *J* = 7.9 Hz, 1H), 7.41 (d, *J* = 8.1 Hz, 1H), 7.25 (dd, *J* = 11.0, 8.2 Hz, 3H), 7.19 – 7.11 (m, 3H), 7.06 (d, *J* = 2.2 Hz, 2H), 3.66 (q, *J* = 6.7 Hz, 2H), 3.26 (t, *J* = 7.4 Hz, 2H), 3.04 (t, *J* = 6.8 Hz, 2H), 2.90 (t, *J* = 7.4 Hz, 2H). **^{13}C NMR (126 MHz, $CDCl_3$): δ** 197.97, 159.88, 138.84, 136.42, 129.77, 128.60, 127.09, 122.38, 122.04, 119.63, 118.63, 112.40, 111.31, 39.46, 38.12, 31.95, 29.70 (d, *J* = 5.0 Hz), 29.38, 28.46, 25.11, 22.71, 14.15. **HRMS (ESI):** m/z calculated for $C_{20}H_{20}ClN_2O_2$ $[M+H]^+$: 355.1213; found : 355.1213. HPLC % Purity: 96.48

5.4.1.1.4. 4-(4-chlorophenyl)-N-(2-(5-methoxy-1H-indol-3-yl)ethyl)-2-oxobutanamide **(MD04)**

Yellow solid, 77% yield **^{1}H NMR (500 MHz, $CDCl_3$): δ** 7.99 (s, 1H), 7.33 – 7.23 (m, 3H), 7.14 (d, *J* = 8.5 Hz, 2H), 7.03 (dd, *J* = 7.4, 2.3 Hz, 3H), 6.90 (dd, *J* = 8.8, 2.5 Hz, 1H), 3.88 (s, 3H), 3.64 (dd, *J* = 13.1, 6.8 Hz, 2H), 3.26 (t, *J* = 7.4 Hz, 2H), 3.00 (t, *J* = 6.8 Hz, 2H), 2.90 (t, *J* = 7.4 Hz, 2H). **^{13}C NMR (126 MHz, $CDCl_3$): δ** 197.98, 159.91, 154.19, 138.84, 132.02, 131.56, 129.76, 129.3, 129.16, 128.66, 127.52, 122.80, 112.60, 112.09, 100.46, 55.95, 44.62, 42.79, 39.43, 38.11, 29.71, 28.46, 25.08, 14.16. **HRMS (ESI)**: m/z calculated for $C_{21}H_{22}ClN_2O_2$ $[M+H]^+$: 385.1319; found : 385.1272

5.4.1.1.5. N-(2-(1H-indol-3-yl)ethyl)-4-(2-fluorophenyl)-2-oxobutanamide **(MD05)**

Yellow solid, 87% yield **^{1}H NMR (500 MHz, $CDCl_3$): δ** 8.10 (s, 1H), 7.62 (d, *J* = 7.9 Hz, 1H), 7.40 (d, *J* = 8.1 Hz, 1H), 7.27 – 7.18 (m, 3H), 7.16 (dd, *J* = 11.0, 4.0 Hz, 1H), 7.09 – 7.04 (m, 3H), 7.02 (dd, *J* = 9.9, 1.4 Hz, 1H), 3.66 (q, *J* = 6.8 Hz, 2H), 3.29 (t, *J* = 7.5 Hz, 2H), 3.04 (t, *J* = 6.9 Hz, 2H), 2.97 (t, *J* = 7.5 Hz, 2H). **^{13}C NMR (126 MHz, $CDCl_3$): δ** 198.01, 162.13, 160.18, 159.92, 136.44, 130.59, 128.09, 127.48, 124.06, 122.36, 122.04, 119.62, 118.64, 115.41, 115.24, 112.44, 111.31, 39.46, 37.07, 29.72, 25.14, 22.75 (d, *J* = 2.8 Hz). **HRMS (ESI)**: m/z calculated for $C_{20}H_{19}FN_2O_2$ $[M+H]^+$: 339.1509; found : 339.1505

5.4.1.1.6. 4-(2-fluorophenyl)-N-(2-(5-methoxy-1H-indol-3-yl)ethyl)-2-oxobutanamide **(MD-06)**

Yellow solid, 74% yield **. ^{1}H NMR (500 MHz, $CDCl_3$): δ** 8.02 (s, 1H), 7.33 – 7.25 (m, 1H), 7.24 – 7.17 (m, 2H), 7.05 (ddd, *J* = 19.5, 10.7, 6.1 Hz, 5H), 6.94 – 6.85 (m, 1H), 3.90 – 3.87 (s, 3H), 3.69 – 3.60 (m, 2H), 3.30 (dd, *J* = 19.5, 12.1 Hz, 4H), 3.04 – 2.91 (m, 2H). **^{13}C NMR (126 MHz, $CDCl_3$): δ** 198.01, 159.93, 154.18, 131.57, 130.59, 128.08, 127.53, 127.23, 124.05, 122.82, 115.41, 115.23, 112.60, 112.11, 100.44, 55.95, 39.60, 39.41, 37.08, 31.94, 29.71,

25.12, 22.74, 14.31, 14.12. **HRMS (ESI):** m/z calculated for $C_{21}H_{21}FN_2O_3$ $[M+H]^+$: 369.1614; found : 369.1610.

5.4.1.1.7. N-(2-(1H-indol-3-yl)ethyl)-4-(2,5-dibromophenyl)-2-oxobutanamide **(MD-07)**

White solid, 79 % yield **^{1}H NMR (500 MHz, $CDCl_3$): δ** 8.11 (s, 1H), 7.62 (d, *J* = 7.9 Hz, 1H), 7.43 – 7.39 (m, 3H), 7.27 – 7.21 (m, 2H), 7.16 (t, *J* = 7.4 Hz, 1H), 7.07 (d, *J* = 2.1 Hz, 2H), 3.67 (q, *J* = 6.8 Hz, 2H), 3.28 (t, *J* = 7.5 Hz, 2H), 3.05 (t, *J* = 6.8 Hz, 2H), 3.00 (t, *J* = 7.5 Hz, 2H). **^{13}C NMR (126 MHz, $CDCl_3$): δ** 197.53, 159.77, 141.86, 136.43, 134.24, 133.34, 131.12, 127.09, 123.04, 122.3, 122.07, 121.28, 119.64, 118.64, 112.39, 111.33, 77.30, 77.04, 76.79, 39.49, 36.61, 31.95, 31.46, 30.21, 29.70, 29.44, 25.13, 22.72, 14.15. **HRMS (ESI)**: m/z calculated for $C_{20}H_{18}Br_2N_2O_2$ $[M+H]^+$: 478.9793; found : 478.9793. HPLC % Purity: 96.48

5.4.1.1.8. 4-(2,5-dibromophenyl)-N-(2-(5-methoxy-1H-indol-3-yl)ethyl)-2-oxobutanamide **(MD-08)**

Yellow solid, 77% yield· **^{1}H NMR (500 MHz, $CDCl_3$): δ** 8.01 (s, 1H), 7.45 – 7.38 (m, 2H), 7.29 (dd, *J* = 4.9, 3.9 Hz, 1H), 7.22 (dd, *J* = 8.5, 2.4 Hz, 1H), 7.09 (s, 1H), 7.04 (d, *J* = 2.3 Hz, 2H), 6.91 (dd, *J* = 8.8, 2.4 Hz, 1H), 3.89 (s, 3H), 3.66 (q, *J* = 6.8 Hz, 2H), 3.28 (t, *J* = 7.5 Hz, 2H), 3.00 (dd, *J* = 12.8, 7.1 Hz, 4H). **^{13}C NMR (126 MHz, $CDCl_3$): δ** 197.54, 159.80, 154.19, 141.86, 134.23, 133.33, 131.56, 131.12, 127.52, 123.03, 122.82, 121.28, 112.62 , 112.10, 100.44 , 55.96, 39.45, 36.61, 29.71, 29.49, 25.14, 14.13 (s). **HRMS (ESI):** m/z calculated for $C_{21}H_{20}Br_2N_2O_2$ $[M+H]^+$: 508.9898; found : 508.9898. HPLC %Purity: 97.56

5.4.1.1.9. N-(2-(1H-indol-3-yl)ethyl)-2-oxo-4-(4-(trifluoromethyl)phenyl)butanamide **(MD-09)**

Yellow solid, 77% yield**. ^{1}H NMR (500 MHz, $CDCl_3$): δ** 8.08 (s, 1H), 7.62 (d, *J* = 7.9 Hz, 1H), 7.55 (d, *J* = 8.1 Hz, 2H), 7.41 (d, *J* = 8.1 Hz, 1H), 7.33 (d, *J* = 8.0 Hz, 2H), 7.27 – 7.21 (m, 1H), 7.15 (t, *J* = 7.9 Hz, 1H), 7.06 (s, 2H), 3.66 (dd, *J* = 13.1, 6.8 Hz, 2H), 3.30 (t, *J* = 7.4

Hz, 2H), 3.04 (t, *J* = 6.8 Hz, 2H), 3.00 (t, *J* = 7.4 Hz, 2H). **^{13}C NMR (126 MHz, $CDCl_3$): δ** 197.75, 159.84, 144.50, 136.44, 128.74, 127.11, 125.43, 122.39, 122.01, 119.64, 118.61, 112.40, 111.31, 39.50, 37.85, 31.94, 29.69, 29.37, 28.88, 25.11, 22.70, 14.12, 1.02. **HRMS (ESI):** m/z calculated for $C_{21}H_{19}F_3N_2O_2$ $[M+H]^+$: 389.1477; found : 389.1465

5.4.1.1.10.N-(2-(5-methoxy-1H-indol-3-yl)ethyl)-2-oxo-4-(4(trifluoromethyl)phenyl)butanamide (**MD-10):**

Yellow solid, 77% yield. **^{1}H NMR (500 MHz, $CDCl_3$): δ** 7.97 (s, 1H), 7.55 (d, *J* = 8.1 Hz, 2H), 7.38 – 7.29 (m, 3H), 7.04 (d, *J* = 9.9 Hz, 3H), 6.91 (dd, *J* = 8.8, 2.4 Hz, 1H), 3.88 (s, 3H), 3.65 (q, *J* = 6.7 Hz, 2H), 3.30 (t, *J* = 7.4 Hz, 2H), 3.00 (dd, *J* = 12.7, 6.8 Hz, 4H). **^{13}C NMR (126 MHz, $CDCl_3$): δ** 197.76, 154.20, 131.56, 128.73, 127.52, 125.43, 122.78, 112.61, 112.09, 100.46, 55.94, 39.44, 37.85, 29.70, 29.36, 28.87, 25.11, 22.70, 14.12. **HRMS (ESI):** m/z calculated for $C_{22}H_{21}F_3N_2O_3$ $[M+H]^+$: 419.1583; found : 419.1575. HPLC % Purity: 98.32

5.4.1.1.11. N-(2-(1H-indol-3-yl)ethyl)-4-(3-nitrophenyl)-2-oxobutanamide **(MD-11)**

Yellow solid, 85% yiel. **^{1}H NMR (500 MHz, $CDCl_3$): δ** 8.13 (s, 1H), 8.08 (d, *J* = 9.0 Hz, 2H), 7.61 (d, *J* = 8.3 Hz, 1H), 7.55 (d, *J* = 7.8 Hz, 1H), 7.50 – 7.43 (m, 1H), 7.40 (d, *J* = 8.1 Hz, 1H), 7.24 (t, *J* = 7.6 Hz, 1H), 7.19 – 7.12 (m, 1H), 7.06 (s, 2H), 3.66 (dd, *J* = 13.1, 6.8 Hz, 2H), 3.33 (t, *J* = 7.3 Hz, 2H), 3.04 (t, *J* = 7.1 Hz, 4H). **^{13}C NMR (126 MHz, $CDCl_3$): δ** 197.48, 159.77, 148.39, 142.42, 136.45, 134.70, 129.41, 127.10, 123.40, 122.38, 122.06, 121.52, 119.62, 118.60, 112.34, 111.34, 39.52, 37.79, 29.71, 28.68, 25.09 , 22.70, 14.12. **HRMS (ESI):** m/z calculated for $C_{20}H_{19}F_3N_3O_4$ $[M+H]^+$: 366.1454; found : 366.1441

5.4.1.1.12. N-(2-(5-methoxy-1H-indol-3-yl)ethyl)-4-(3-nitrophenyl)-2-oxobutanamide **(MD-12)**

Yellow solid, 85% yield· **^{1}H NMR (500 MHz, $CDCl_3$): δ** 8.08 (d, *J* = 10.1 Hz, 2H), 8.02 (s, 1H), 7.55 (d, *J* = 7.7 Hz, 1H), 7.46 (t, *J* = 8.0 Hz, 1H), 7.29 (d, *J* = 8.7 Hz, 2H), 7.12 – 6.98 (m,

3H), 6.90 (dd, *J* = 8.8, 2.4 Hz, 1H), 3.92 – 3.84 (m, 3H), 3.65 (dd, *J* = 13.1, 6.8 Hz, 2H), 3.33 (t, *J* = 7.3 Hz, 2H), 3.02 (dt, *J* = 13.5, 7.1 Hz, 4H**). ^{13}C NMR (126 MHz, $CDCl_3$): δ** 197.50, 159.78, 154.18, 148.39, 142.42, 134.70, 131.57, 129.41, 127.51, 123.39, 122.82, 121.52, 112.58, 112.07, 100.46, 55.95, 39.45, 37.80, 29.70, 28.68, 25.10. **HRMS (ESI)**: m/z calculated for $C_{21}H_{21}N_3O_5$ $[M+H]^+$: 396.1559; found : 396.1556

5.4.1.1.13. 1-(4-(4-nitrophenyl)piperazin-1-yl)-4-phenylbutane-1,2-dione **(MD-13)**

Yellow solid, 92 % yield. **^{1}H NMR (500 MHz, $CDCl_3$): δ** 8.17 (d, *J* = 9.4 Hz, 2H), 7.35 – 7.29 (m, 2H), 7.27 – 7.20 (m, 3H), 6.83 (d, *J* = 9.4 Hz, 2H), 3.82 – 3.75 (m, 2H), 3.52 – 3.43 (m, 4H), 3.31 (dd, *J* = 6.3, 4.2 Hz, 2H), 3.21 (t, *J* = 7.3 Hz, 2H), 3.04 (t, *J* = 7.3 Hz, 2H). **^{13}C NMR (126 MHz, $CDCl_3$): δ** 199.91, 164.78, 154.31, 139.99 , 139.46, 128.64, 128.41, 126.50, 125.93, 113.35, 47.37, 46.78, 44.64, 41.14, 29.71, 29.02. **HRMS (ESI):** m/z calculated for $C_{20}H_{21}N_3O_4$ $[M+H]^+$: 368.1610; found : 368.1607

5.4.1.1.14. 1-(4-(2,5-dimethylphenyl)piperazines-1-yl)-4-phenylbutane-1,2-dione **(MD-14)**

Yellow liquid, 82 % yield**. ^{1}H NMR (500 MHz, $CDCl_3$): δ** 7.32 (t, *J* = 7.5 Hz, 2H), 7.25 (dt, *J* = 17.2, 8.7 Hz, 3H), 7.10 (d, *J* = 7.6 Hz, 1H), 6.87 (d, *J* = 7.6 Hz, 1H), 6.79 (s, 1H), 3.77 (s, 2H), 3.45 – 3.38 (m, 2H), 3.19 (t, *J* = 7.4 Hz, 2H), 3.05 (t, *J* = 7.4 Hz, 2H), 2.95 – 2.88 (m, 2H), 2.84 – 2.74 (m, 2H), 2.33 (s, 3H), 2.28 (s, 3H). **^{13}C NMR (126 MHz, $CDCl_3$): δ** 200.37, 165.38, 150.46, 140.15, 136.34, 131.01, 129.45, 128.68 – 128.31, 126.40, 126.13, 124.63, 120.13, 51.99, 51.56, 46.11, 42.12, 41.41, 36.72, 29.71, 28.97, 21.13, 17.31. **HRMS (ESI):** m/z calculated for $C_{22}H_{26}N_2O_2$ $[M+H]^+$: 351.2073; found : 351.2072

5.4.1.1.15. 2-(4-(2-oxo-4-phenylbutanoyl)piperazin-1-yl)benzonitrile **(MD_15)**

Yellow liquid, 72 % yield**. ^{1}H NMR (500 MHz, $CDCl_3$): δ** 7.62 (d, *J* = 9.0 Hz, 1H), 7.54 (t, *J* = 7.9 Hz, 1H), 7.31 (dd, *J* = 15.6, 8.2 Hz, 2H), 7.27 – 7.18 (m, 3H), 7.11 (t, *J* = 7.6 Hz, 1H), 7.00 (d, *J* = 8.3 Hz, 1H), 3.86 – 3.80 (m, 2H), 3.51 – 3.43 (m, 2H), 3.26 – 3.15 (m, 4H), 3.11 –

3.06 (m, 2H), 3.04 (t, *J* = 7.4 Hz, 2H). **^{13}C NMR (126 MHz, $CDCl_3$): δ** 200.17, 165.23, 154.95, 140.04, 134.33, 133.95, 128.62, 128.39, 126.46, 122.92, 119.11, 117.93, 106.96, 77.28, 77.03, 76.77, 51.87, 51.30, 45.66, 41.74, 41.31, 29.70, 28.97. **HRMS (ESI):** m/z calculated for $C_{21}H_{21}N_3O_2$ $[M+H]^+$: 348.1712; found : 348.1710

5.4.1.1.16. 4-(4-chlorophenyl)-1-(4-(4-nitrophenyl)piperazin-1-yl)butane-1,2-dione **(MD-16)**

Yellow solid, 77% yield**. ^{1}H NMR (500 MHz, $CDCl_3$): δ** 8.14 (d, *J* = 9.3 Hz, 2H), 7.28 – 7.23 (m, 2H), 7.15 (d, *J* = 8.5 Hz, 2H), 6.82 (d, *J* = 9.4 Hz, 2H), 3.79 – 3.75 (m, 2H), 3.54 – 3.50 (m, 2H), 3.48 – 3.44 (m, 2H), 3.37 – 3.31 (m, 2H), 3.16 (t, *J* = 7.3 Hz, 2H), 2.97 (t, *J* = 7.3 Hz, 2H). **^{13}C NMR (126 MHz, $CDCl_3$): δ** 199.39, 164.55, 154.30, 139.52, 138.51, 132.28, 129.79, 128.73, 125.93, 113.40, 47.41, 46.81, 44.75, 41.25, 41.03, 29.70, 28.34. **HRMS (ESI):** m/z calculated for $C_{20}H_{20}ClN_3O_4$ $[M+H]^+$: 402.1221; found 402.1222

5.4.1.1.17. 4-(2,5-dibromophenyl)-1-(4-(4-nitrophenyl)piperazin-1-yl)butane-1,2-dione **(MD17)**

Yellow solid, 77% yield **. ^{1}H NMR (500 MHz, $CDCl_3$): δ** 8.23 – 8.14 (m, 2H), 7.42 (dd, *J* = 15.4, 7.0 Hz, 2H), 7.25 (dd, *J* = 8.4, 2.1 Hz, 1H), 6.87 (d, *J* = 9.3 Hz, 2H), 3.88 – 3.77 (m, 2H), 3.71 – 3.63 (m, 2H), 3.54 – 3.49 (m, 2H), 3.49 – 3.44 (m, 2H), 3.22 (t, *J* = 7.4 Hz, 2H), 3.09 (t, *J* = 7.4 Hz, 2H). **^{13}C NMR (126 MHz, $CDCl_3$): δ** 198.83, 164.31, 154.30, 141.51, 134.34, 133.28, 131.28, 125.94, 122.98, 121.37, 113.41, 47.51, 46.83, 44.88, 41.34, 39.39, 37.10, 31.93 , 30.04, 29.70, 29.31, 22.70, 14.1. **HRMS (ESI):** m/z calculated for $C_{20}H_{19}Br_2N_3O_4$ $[M+H]^+$: 525.9800; found 525.9800

5.4.1.1.18. 1-(4-(4-nitrophenyl)piperazin-1-yl)-4-(4-(trifluoromethyl)phenyl)butane-1,2-dione **(MD-18)**

Yellow liquid **^{1}H NMR (500 MHz, $CDCl_3$): δ** 8.15 – 8.06 (m, 1H), 7.54 (d, *J* = 8.1 Hz, 1H), 7.34 (d, *J* = 8.0 Hz, 1H), 6.86 – 6.76 (m, 1H), 3.78 (dd, *J* = 6.2, 4.5 Hz, 1H), 3.55 (dd,

J = 6.2, 4.3 Hz, 1H), 3.46 (dd, *J* = 6.2, 4.5 Hz, 1H), 3.39 – 3.31 (m, 1H), 3.21 (t, *J* = 7.2 Hz, 1H), 3.05 (t, *J* = 7.3 Hz, 1H). **^{13}C NMR (126 MHz, $CDCl_3$): δ** 199.07, 164.44, 154.28, 144.26, 139.42, 129.22, 128.96, 128.78, 128.70, 128.44, 125.91, 125.56, 125.53, 125.50, 125.47, 125.26, 123.10, 113.32, 47.37, 46.74, 44.76, 41.28, 40.77, 29.69, 28.71, 22.68. **HRMS (ESI):** m/z calculated for $C_{21}H_{20}F_3N_3O_4$ $[M+H]^+$: 436.1484; found 436.1485

5.4.1.1.19. 4-(2-fluorophenyl)-1-(4-(4-nitrophenyl)piperazin-1-yl)butane-1,2-dione **(MD-19)**

Yellow solid, 75% yield **^{1}H NMR (500 MHz, CDCl3): δ** 8.17 (d, J = 9.3 Hz, 2H), 7.23 (dd, J = 16.5, 8.5 Hz, 2H), 7.05 (dd, J = 18.5, 8.7 Hz, 2H), 6.85 (d, J = 9.4 Hz, 2H), 3.85 – 3.76 (m, 2H), 3.64 – 3.53 (m, 2H), 3.54 – 3.47 (m, 2H), 3.44 – 3.37 (m, 2H), 3.21 (t, J = 7.3 Hz, 2H), 3.05 (t, J = 7.3 Hz, 2H). **^{13}C NMR (126 MHz, $CDCl_3$): δ** 199.47, 164.58, 154.32, 139.50, 130.69, 128.32, 125.94, 124.19, 115.50, 115.33, 113.38, 47.46, 46.82, 44.76, 41.23, 39.92, 22.65. **HRMS (ESI**): m/z calculated for $C_{20}H_{20}FN_3O_4$ $[M+H]^+$: 386.1516; found 386.1517

5.4.1.1.20.. 1-(4-(2,5-dimethylphenyl)piperazin-1-yl)-4-(2-fluorophenyl)butane-1,2-dione **(MD_20)**

White solid, 93% yield **^{1}H NMR (500 MHz, $CDCl_3$): δ** 7.28 (t, *J* = 6.8 Hz, 1H), 7.25 – 7.19 (m, 1H), 7.10 (d, *J* = 7.5 Hz, 2H), 7.05 (dd, *J* = 16.7, 7.7 Hz, 1H), 6.87 (d, *J* = 7.6 Hz, 1H), 6.81 (s, 1H), 3.82 – 3.73 (m, 2H), 3.53 – 3.44 (m, 2H), 3.19 (t, *J* = 7.4 Hz, 2H), 3.06 (t, *J* = 7.4 Hz, 2H), 2.97 – 2.90 (m, 2H), 2.89 – 2.83 (m, 2H), 2.33 (s, 3H), 2.29 (s, 3H). **^{13}C NMR (126 MHz, $CDCl_3$): δ** 200.02, 165.24, 162.13, 160.18, 150.46, 136.35, 131.02, 130.71, 129.45, 128.22, 127.04, 124.65, 124.15, 120.14, 115.46, 115.29, 52.04, 51.56, 46.18, 42.16, 40.06, 29.71, 22.61, 21.14, 17.33. **HRMS (ESI):** m/z calculated for $C_{22}H_{25}FN_2O_2$ $[M+H]^+$: 369.1978; found 369.1957

5.4.1.1.21. 2-(4-(4-(2-fluorophenyl)-2-oxobutanoyl)piperazin-1-yl)benzonitrile **(MD-21)**

Yellow liquid, 77% yield. **^{1}H NMR (500 MHz, $CDCl_3$): δ** 7.61 (dd, *J* = 7.7, 1.5 Hz, 1H), 7.56

– 7.50 (m, 1H), 7.23 (tdd, *J* = 9.5, 9.0, 5.5 Hz, 2H), 7.08 (dt, *J* = 7.5, 4.3 Hz, 2H), 7.06 – 6.99 (m, 2H), 3.89 – 3.79 (m, 2H), 3.60 – 3.53 (m, 2H), 3.21 (dd, *J* = 10.1, 5.1 Hz, 2H), 3.19 – 3.12 (m, 2H), 3.03 (t, *J* = 7.4 Hz, 2H). **^{13}C NMR (126 MHz, $CDCl_3$): δ** 199.79, 165.08, 162.09, 160.14, 154.94, 134.32, 133.97, 130.68, 128.28, 126.94, 124.18, 122.94, 119.14, 117.95, 115.47, 115.30, 106.92, 51.94, 51.28, 45.73, 41.78, 39.98, 29.69, 22.60. **HRMS (ESI):** m/z calculated for $C_{21}H_{20}FN_3O_2$ $[M+H]^+$: 366.1618; found : 366.1606

5.4.1.1.22. 4-(3-nitrophenyl)-1-(4-(4-nitrophenyl)piperazin-1-yl)butane-1,2-dion**e (MD-22)**

Yellow solid, 85 % yield **^{1}H NMR (500 MHz, $CDCl_3$): δ** 8.14 (d, *J* = 9.3 Hz, 2H), 8.08 (d, *J* = 6.5 Hz, 2H), 7.58 (d, *J* = 7.6 Hz, 1H), 7.52 – 7.43 (m, 1H), 6.83 (d, *J* = 12.6 Hz, 2H), 3.86 – 3.77 (m, 2H), 3.68 – 3.62 (m, 2H), 3.51 – 3.46 (m, 2H), 3.46 – 3.40 (m, 2H), 3.26 (t, *J* = 7.2 Hz, 2H), 3.11 (t, *J* = 7.2 Hz, 2H). **^{13}C NMR (126 MHz, $CDCl_3$): δ** 198.61, 164.18, 154.28, 148.44, 142.14, 139.54, 134.75, 129.55, 125.94, 123.17, 121.66, 113.41, 47.50, 46.81, 44.89, 41.41, 40.65, 29.70, 28.48**. HRMS (ESI):** m/z calculated for $C_{20}H_{20}FN_4O_6$ $[M+H]^+$: 413.1461; found 413,1446

5.4.1.1.23. 1-(4-(2,5-dimethylphenyl)piperazin-1-yl)-4-(3-nitrophenyl)butane-1,2-dione **(MD-23)**

Yellow liquid, 76% yield· **^{1}H NMR (500 MHz, $CDCl_3$): δ** 8.17 – 8.06 (m, 2H), 7.61 (d, *J* = 7.6 Hz, 1H), 7.50 (t, *J* = 7.9 Hz, 1H), 7.10 (d, *J* = 7.6 Hz, 1H), 6.86 (d, *J* = 7.6 Hz, 1H), 6.80 (s, 1H), 3.84 – 3.75 (m, 2H), 3.59 – 3.53 (m, 2H), 3.25 (t, *J* = 7.4 Hz, 2H), 3.14 (t, *J* = 7.3 Hz, 2H), 2.97 – 2.91 (m, 2H), 2.91 – 2.86 (m, 2H), 2.32 (s, 3H), 2.28 (s, 3H). **^{13}C NMR (126 MHz, $CDCl_3$): δ** 199.12, 164.84, 150.36, 148.45, 142.27, 136.38, 134.74, 131.04, 129.48, 124.71, 123.24, 121.60, 120.12, 52.07, 51.58, 46.30, 42.32, 40.82, 29.71, 28.50, 22.70, 21.13, 17.32, 14.12. **HRMS (ESI)**: m/z calculated for $C_{22}H_{25}N_3O_4$, $[M+H]^+$: 396.1923; found 396.1906

5.4.1.1.24. 2-(4-(4-(3-nitrophenyl)-2-oxobutanoyl)piperazin-1-yl)benzonitrile **(MD-24)**

Yellow liquid, 88% yield . **^{1}H NMR (500 MHz, $CDCl_3$): δ** 8.17 – 8.03 (m, 2H), 7.61 (t, *J* = 7.1 Hz, 2H), 7.51 (dt, *J* = 21.0, 8.0 Hz, 2H), 7.11 (t, *J* = 7.6 Hz, 1H), 7.02 (d, *J* = 8.3 Hz, 1H), 3.90 – 3.82 (m, 2H), 3.69 – 3.60 (m, 2H), 3.29 – 3.21 (m, 4H), 3.22 – 3.16 (m, 2H), 3.13 (t, *J* = 7.3 Hz, 2H). **^{13}C NMR (126 MHz, CDCl3): δ** 198.92, 164.71, 154.87, 148.43, 142.20, 134.73, 134.32, 134.01, 129.53, 123.22, 123.01, 121.62, 119.15, 117.95, 106.95, 51.96, 51.30, 45.87, 41.95, 40, 29.69, 28.47. **HRMS (ESI):** m/z calculated for $C_{21}H_{20}N_4O_4$, $[M+H]^+$: 393.1563; found 393.1543

5.4.2. In vitro Biological evaluation

5.4.2.1. In vitro Aβ aggregation assay

It was performed using the same method as discussed in the **chapter 4, Section 4.4.2.1**

5.4.2.2. In vitro Heparin-Induced Tau Aggregation Assay

It was performed using the same method as discussed in the **Chapter 4, Section 4.4.2.3**

5.4.3. In vivo study Aβ-induced memory impairment in mice

5.4.3.1. **Experimental animals**

It is same as discussed in the **Chapter 4, Section 4.4.3.1**

5.4.3.2. **Drug treatment**

In the present study, we adopted a drug treatment strategy similar to that previously described as detailed in **Chapter 4, Section 4.4.3.2**. However, a modification was made in the dosing of compound MD08. Specifically, MD08 was administered via intraperitoneal (*i.p*) injection at dosages of 2, 5, and 10 mg/kg.

5.4.3.3. Learning and memory test

It was performed using the same method as discussed in the **Chapter 4, Section 4.4.3. 3**

5.4.3.4. Motor coordination

It was performed using the same method as discussed in the **Chapter 4, Section 4.4.3.4**

5.4.3.5. Novel object recognition test

It was performed using the same method as discussed in the **Chapter 4, Section 4.4.3.5**

5.4.4. Solubility Determination

It was performed using the same method discussed in the **Chapter 4, Section 4.4.4.**

5.4.5. PAMPA Assay

The assay was performed by using same protocol as detailed in **Chapter 4, Section 4.4.5**

5.4.6. Computational details

5.4.6.1. In silico study Pharmacokinetic properties

The in silico ADME study was performed by using Swiss ASME webserver, detailed in **Chapter 4** (**Section 4.4.6**)

5.4.6.2. Molecular Docking

The methods for molecular docking discussed in the **Chapter 3 (Section 3.3.5) and Chapter 4 (Section 4.4.6.2)**

5.4.6.3. Molecular Dynamics

The methods for molecular dynamics simulation as detailed in the **Chapter 3** (**Section 3.3.6**)

5.4.6.4. Quantum Chemical calculations

The methods for quantum chemical calculation as detailed in the **Chapter 3** (**Section 3.3.5**)

5.5. Conclusion

The present study involved the synthesis and characterization of a series of twenty-four compounds, which were subsequently characterized using both NMR and HRMS techniques. On their evaluation in a ThT based Aβ aggregation assay, several of them were able to modulate

Aβ aggregation kinetics. Notably, compound MD08 emerged as a particularly potent molecule in this context. Pharmacokinetic studies further elucidated the solubility and permeability characteristics of compound MD08. Additionally, at a concentration of 100 μM, MD08 exhibited the capacity to inhibit the heparin-induced tau protein aggregation. This inhibitory effect was magnified when the concentration was raised to 200 μM, indicating a dose-dependent inhibition of tau aggregation. Cytotoxicity assays conducted using MTT assay in SHSY5Y cell line didn't show any major toxicity. Further in vivo studies conducted on Aβ-injected models suggested that compound MD08 may enhance cognitive functions, especially when administered at a dosage of 10 mg/kg. An in silico ADME assessment was conducted on all the compounds, shedding light on the various drug-like properties of the synthesized molecules. Additionally, molecular docking and dynamic studies provided insights into the binding interactions and the stability of the ligand when in the presence of Aβ and tau peptides. Quantum chemical calculations pertaining to MD08 also elucidated its electronic and thermal properties. To conclude, this study accentuates the potential of MD08 as a noteworthy lead compound, meriting further exploration and development. Additionally, the findings strongly advocate for a comprehensive investigation into the heterocyclic derivatives of α-ketoamides as prospective therapeutic agents against AD.

5.6. References

1. Suliphuldevara Mathada, N. Gunavanthrao Yernale, J.N. Basha, The Multi-Pharmacological Targeted Role of Indole and its Derivatives: A review, ChemistrySelect, 8 (2023) e202204181.
2. Y. Ji, W. Yin, Y. Liang, L. Sun, Y. Yin, W. Zhang, Anti-inflammatory and anti-oxidative activity of indole-3-acetic acid involves induction of HO-1 and neutralization of free radicals in RAW264. 7 cells, International journal of molecular sciences, 21 (2020) 1579.
3. L. Jones, D.S.P. Abdalla, J. Freitas, Effects of indole-3-acetic acid on croton oil-and arachidonic acid-induced mouse ear edema, Inflammation Research, 44 (1995) 372-375.
4. A. Feral, A.R. Martin, A. Desfoux, M. Amblard, L.L. Vezenkov, Covalent-reversible peptide-based protease inhibitors. Design, synthesis, and clinical success stories, Amino Acids, (2023) 1-26.

5. K. Savonije, D.F. Weaver, The Role of Tryptophan Metabolism in Alzheimer's Disease, Brain Sciences, 13 (2023) 292.
6. S.S. Durairajan, K. Selvarasu, M.R. Bera, K. Rajaram, A. Iyaswamy, M. Li, Alzheimer's disease and other tauopathies: exploring efficacy of medicinal plant-derived compounds in alleviating tau-mediated neurodegeneration, Current Molecular Pharmacology, 15 (2022) 361-379.
7. A. Więckowska, N. Szałaj, I. Góral, A. Bucki, G. Latacz, K. Kiec-Kononowicz, Ò.M. Bautista-Aguilera, A. Romero, E. Ramos, J. Egea, V. Farré Alíns, Á. González-Rodríguez, F. López-Muñoz, M. Chioua, J. Marco-Contelles, In Vitro and In Silico ADME-Tox Profiling and Safety Significance of Multifunctional Monoamine Oxidase Inhibitors Targeting Neurodegenerative Diseases, ACS Chemical Neuroscience, 11 (2020) 3793-3801.
8. P.S. Girase, S. Dhawan, V. Kumar, S.R. Shinde, M.B. Palkar, R. Karpoormath, An appraisal of anti-mycobacterial activity with structure-activity relationship of piperazine and its analogues: A review, European Journal of Medicinal Chemistry, 210 (2021) 112967.
9. R.R. Kumar, B. Sahu, S. Pathania, P.K. Singh, M.J. Akhtar, B. Kumar, Piperazine, a Key Substructure for Antidepressants: Its Role in Developments and Structure-Activity Relationships, ChemMedChem, 16 (2021) 1878-1901.
10. S.M. Sanad, A.E. Mekky, Ultrasound-Mediated Synthesis of New (Piperazine-Chromene)-Linked Bis (thieno [2, 3-b] pyridine) Hybrids as Potential Anti-acetylcholinesterase, ChemistrySelect, 7 (2022) e202203020.
11. B.-B. Wei, C. Han, P.-P. Shang, X.-Y. Guo, L.-G. Bai, Z.-Y. Ma, Design, synthesis and assay of 2-(4-phenylpiperazin-1-yl) pyrimidine-5-carboxamide derivatives as acetylcholinesterase inhibitors, Medicinal Chemistry Research, 31 (2022) 1901-1915.
12. K. Walayat, S. Aslam, N. Rasool, M. Ahmad, A. Rafiq, S.A. Al-Hussain, M.E. Zaki, Recent Advances in the Piperazine Based Antiviral Agents: A Remarkable Heterocycle for Antiviral Research, Arabian Journal of Chemistry, (2023) 105292.
13. B. Das, A.T. Baidya, B. Devi, T. Rom, A.K. Paul, B. Thakur, T. Darreh-Shori, R. Kumar, Synthesis, single crystal X-ray, DFT, spectroscopic, molecular docking studies and in vitro biological evaluation of compound N-benzyl-4-(4-chlorophenyl)-2-oxobutanamide, Journal of Molecular Structure, 1276 (2023) 134782.
14. R. Maity, B. Das, I. Das, Transition-Metal-Free Reduction of α-Keto Thioesters with Hydrosilanes at Room Temperature: Divergent Synthesis through Reagent-Controlled Chemoselectivities, Advanced Synthesis & Catalysis, 361 (2019) 2347-2353.